Sensitivity of a Coarse-Resolution Global Ocean Model to Spatially Variable Neutral Diffusion

Ryan M Holmes[1], Sjoerd Groeskamp[2], Kial Douglas Stewart[3], and Trevor John McDougall[4]

[1]University of Sydney
[2]Royal Netherlands Institute for Sea Research
[3]Australian National University
[4]The School of Mathematics and Statistics, University of New South Wales

November 24, 2022

Abstract

Motivated by recent advances in mapping mesoscale eddy tracer mixing in the ocean we evaluate the sensitivity of a coarse-resolution global ocean model to a spatially variable neutral diffusion coefficient $\kappa_n(x,y,z)$. We gradually introduce physically-motivated models for the horizontal (mixing length theory) and vertical (surface mode theory) structure of κ_n along with suppression of mixing by mean flows. Each structural feature influences the ocean's hydrography and circulation to varying extents, with the suppression of mixing by mean flows being the most important factor and the vertical structure being relatively unimportant. When utilizing the full theory (experiment "FULL') the interhemispheric overturning cell is strengthened by 2 Sv at 26°N (a $\sim20\%$ increase), bringing it into better agreement with observations. Zonal mean tracer biases are also reduced in FULL. Neutral diffusion impacts circulation through surface temperature-induced changes in surface buoyancy fluxes and non-linear equation of state effects. Surface buoyancy forcing anomalies are largest in the Southern Ocean where decreased neutral diffusion in FULL leads to surface cooling and enhanced dense-to-light surface watermass transformation, reinforced by reductions in cabbeling and thermobaricity. The increased watermass transformation leads to enhanced mid-latitude stratification and interhemispheric overturning. The spatial structure for κ_n in FULL is important as it enhances the interhemispheric cell without degrading the Antarctic bottom water cell, unlike a spatially-uniform reduction in κ_n. These results highlight the sensitivity of modeled circulation to κ_n and motivate the use of physics-based models for its structure.

Sensitivity of a Coarse-Resolution Global Ocean Model to Spatially Variable Neutral Diffusion

R. M. Holmes[1,2,3,4], S. Groeskamp[5], K.D. Stewart[3,6] and T.J. McDougall[4]

[1]School of Geosciences, University of Sydney, Sydney, Australia
[2]Climate Change Research Centre, University of New South Wales, Sydney, Australia
[3]Australian Research Council Centre of Excellence for Climate Extremes, Australia
[4]School of Mathematics and Statistics, University of New South Wales, Sydney, Australia
[5]NIOZ Royal Netherlands Institute for Sea Research, Texel, The Netherlands
[6]Research School of Earth Sciences, Australian National University, Canberra, Australia

Key Points:

- A new spatially-variable parameterization for mesoscale neutraldiffusion is tested in a 1-degree ocean model
- Both hydrography and circulation are sensitive to the magnitude and spatial structure of neutral diffusion
- A 2Sv enhancement in interhemispheric overturning stems from suppression of neutral diffusion by mean flows

Corresponding author: Ryan Holmes, `r.holmes@sydney.edu.au`

Abstract

Motivated by recent advances in mapping mesoscale eddy tracer mixing in the ocean we evaluate the sensitivity of a coarse-resolution global ocean model to a spatially variable neutral diffusion coefficient $\kappa_n(x, y, z)$. We gradually introduce physically-motivated models for the horizontal (mixing length theory) and vertical (surface mode theory) structure of κ_n along with suppression of mixing by mean flows. Each structural feature influences the ocean's hydrography and circulation to varying extents, with the suppression of mixing by mean flows being the most important factor and the vertical structure being relatively unimportant. When utilizing the full theory (experiment "FULL") the interhemispheric overturning cell is strengthened by 2 Sv at 26°N (a $\sim 20\%$ increase), bringing it into better agreement with observations. Zonal mean tracer biases are also reduced in FULL. Neutral diffusion impacts circulation through surface temperature-induced changes in surface buoyancy fluxes and non-linear equation of state effects. Surface buoyancy forcing anomalies are largest in the Southern Ocean where decreased neutral diffusion in FULL leads to surface cooling and enhanced dense-to-light surface watermass transformation, reinforced by reductions in cabbeling and thermobaricity. The increased watermass transformation leads to enhanced mid-latitude stratification and interhemispheric overturning. The spatial structure for κ_n in FULL is important as it enhances the interhemispheric cell without degrading the Antarctic bottom water cell, unlike a spatially-uniform reduction in κ_n. These results highlight the sensitivity of modeled circulation to κ_n and motivate the use of physics-based models for its structure.

Plain Language Summary:

The diffusion of tracers such as temperature and salinity along surfaces of constant density by the action of mesoscale eddy stirring, known as neutral diffusion, is an important transport process in the ocean which impacts heat, carbon and nutrient budgets as well as climate variability. However, most global ocean circulation models used for climate studies have a horizontal grid resolution that is too coarse to resolve mesoscale eddies. Thus, the effects of eddy-driven neutral diffusion must be parameterized through the inclusion of a neutral diffusivity parameter κ_n. While the strength of neutral diffusion is known to vary spatially within the ocean, most models still make simple choices for κ_n; a constant, or scaled according to the grid resolution. In this study, we examine the sensitivity of a coarse-resolution global ocean model to the spatial structure of κ_n using a recently developed and physically-motivated three-dimensional mapping of mesoscale mixing. Our results show that the modeled meridional overturning circulation and tracer structure are sensitive to both the magnitude and the spatial structure of κ_n, suggesting that more attention should be paid to this parameter in future model development.

1 Introduction

The diffusion of tracers along neutral density surfaces through the action of mesoscale eddy stirring, or "neutral diffusion", is an important transport process in the ocean that influences the heat, salt, carbon and nutrient budgets, ocean ventilation, deep and bottom water formation and climate variability (e.g. Busecke & Abernathey, 2019; England & Rahmstorf, 1999; Gnanadesikan et al., 2015; Griffies et al., 2015; Jones & Abernathey, 2019, 2021; Morrison et al., 2013; Sijp et al., 2006; Sijp & England, 2009; Williams et al., 2007; Wolfe et al., 2008). Mesoscale eddies are poorly represented in the global coarse-resolution models used for many climate studies and thus the associated neutral diffusion must be parameterized through the inclusion of an explicit neutral diffusivity, κ_n. Despite significant advances in theory, the spatial and temporal structure of κ_n is poorly understood and many models still make simple choices for κ_n based on ad-hoc, rather than physical, reasoning (e.g. see Table 1 of Meijers (2014) for a summary of neutral physics choices in CMIP5 models). The choice of κ_n has implications for the model representation of a large range of processes of climatic relevance (e.g. Ferreira et al., 2005; Gnanadesikan et al., 2017; Pradal & Gnanadesikan, 2014) and is likely to remain a first-order issue for some time given that higher resolution, eddy-resolving coupled models are still impractical for many applications. In this study, we take advantage of recent advancements in the mapping of mesoscale mixing in the ocean based on theory and observations (Groeskamp et al., 2020) to revisit this issue using a coarse-resolution global ocean model.

Since the step-change improvement in non eddy-resolving ocean models associated with the work of Gent and McWilliams (1990) (hereafter GM) and the movement away from simple horizontal diffusive closures (due to the detrimental "Veronis effect", Gough & Lin, 1995; McDougall & Church, 1986; Veronis, 1975) toward rotated along-isopycnal or neutral diffusion (Griffies et al., 1998; McDougall et al., 2014; Redi, 1982; Solomon, 1971), how to choose the GM coefficient, κ_{GM}, and the neutral tracer diffusivity, κ_n, has become an important topic of research. A range of theories have been developed, most of which focus primarily on the adiabatic eddy-driven circulation represented by κ_{GM} (e.g. Cessi, 2008; Eden & Greatbatch, 2008; Eden et al., 2009; Jansen et al., 2019, 2015; Jansen & Held, 2014; Marshall & Adcroft, 2010; Pearson et al., 2017; Smith & Vallis, 2002; Treguier et al., 1997; Visbeck et al., 1997). Some of these schemes are based on energy conservation and consider the effects of mesoscale eddies in the momentum budget (e.g. Eden & Greatbatch, 2008; Jansen et al., 2019; Jansen & Held, 2014; Juricke et al., 2020). However, the independent choice of the neutral diffusivity κ_n has received less attention. While some models make the choice $\kappa_n = \kappa_{GM}$, theory and diagnostics from high-resolution models and field experiments suggests that the two may be quite different (e.g. Abernathey et al., 2013, 2010; Smith & Marshall, 2009; Vollmer & Eden, 2013). Experience with model tuning suggests that the choice $\kappa_n = \kappa_{GM}$ can be problematic and thus many models that use sophisticated flow-dependent schemes for κ_{GM} retain simple ad-hoc choices (often constant, or scaled according to the grid spacing) for κ_n not necessarily based on physical reasoning (e.g. Gnanadesikan et al., 2006; Griffies et al., 2004; Johns et al., 2006; Jungclaus et al., 2010; Voldoire et al., 2013).

Documentation of the independent sensitivity of coarse-resolution climate simulations to κ_n remains limited, despite the model tuning performed behind the scenes at modeling centers. While κ_{GM} is known to have strong impacts on the ocean's overturning circulation and the Antarctic Circumpolar Current (ACC) strength, κ_n may be just as important as κ_{GM} for determining thermocline stratification and abyssal tracer distributions (e.g. Danabasoglu & McWilliams, 1995). Danabasoglu and Marshall (2007) showed improvements in upper-ocean temperature biases and heat transport in their coarse-resolution simulations when the vertical structure of κ_{GM} was surface-intensified. Introducing a similar vertical structure in κ_n showed small additional improvements. Coupled model studies show that large ($\sim 600\%$) changes in a spatially-uniform κ_n can have significant impacts on high-latitude processes, where along-isopycnal temperature and salinity gradients are typically largest, including sea-ice formation, surface fluxes, stratification and deep convection (Pradal & Gnanadesikan, 2014; Sijp et al., 2006; Sijp & England, 2009). κ_n is also thought to influence tropical climate variability (Gnanadesikan et al., 2017). We also note recent studies recommending that anisotropic effects, that are not addressed here, should be taken into account (Bachman et al., 2020; Stanley et al., 2020).

In this article we isolate the sensitivity of a coarse-resolution ocean model to κ_n, independently of κ_{GM}, using the theory- and observation-based three-dimensional maps of κ_n recently constructed by Groeskamp et al. (2020). As a sensitivity test, we consider only static maps of κ_n, leaving the development of a dynamic parameterization better suited to production use for future studies. We separate the impacts of the various structural ingredients included in Groeskamp et al. (2020)'s κ_n; the mixing length theory that governs the horizontal structure, the surface mode theory that governs the vertical struc-

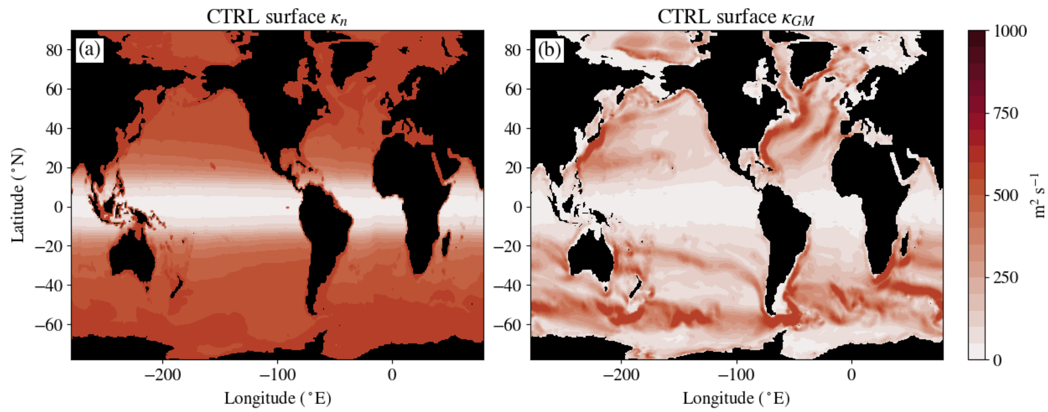

Figure 1. (a) The structure of κ_n in the ACCESS-OM2 control simulation (CTRL) indicating the impact of the grid-scaling factor [Eq. (4)]. (b) The two-dimensional time-averaged spatial structure of κ_{GM} from CTRL determined according to the "baroclinic zone" dynamical setting of Griffies (2012); Griffies et al. (2005) and a maximum (minimum) of 600 $\mathrm{m^2\ s^{-1}}$ (50 $\mathrm{m^2\ s^{-1}}$) used for all experiments.

ture (LaCasce, 2017) and the suppression of mixing by mean flows (Ferrari & Nikurashin, 2010). The use of an ocean-only model, rather than a coupled climate model, allows a clean attribution of cause and effect, avoiding runaway air-sea feedbacks. In such a system where the wind-forcing is fixed, the impact of variations in κ_n on the interior buoyancy structure and thus circulation should only arise through changes in surface heat and buoyancy fluxes (e.g. Guilyardi et al., 2001; Hieronymus & Nycander, 2013) or non-linear equation of state effects such as cabbeling and thermobaricity (Klocker & McDougall, 2010; McDougall, 1987). Our model and experimental design, along with a brief summary of the κ_n theory of Groeskamp et al. (2020), is presented in Section 2.1. Section 3 presents an analysis of the sensitivity of the meridional overturning circulation (MOC) and tracer distributions to κ_n, along with a discussion of the associated mechanisms. Section 4 summarizes our results and discusses drawbacks and next steps.

2 Methods

2.1 The global ocean sea-ice model

We use the coarse 1° horizontal resolution configuration of the global ocean sea-ice model ACCESS-OM2 (Kiss et al., 2020), which couples together the Modular Ocean Model version 5.1 (MOM5, Griffies, 2012) and the Los Alamos Sea Ice Model version 5.1.2 (CICE, Hunke et al., 2015). Forcing is taken from the JRA55-do reanalysis (Tsujino et al., 2018) and consists of a repeating cycle of the period May 1990 to April 1991 (Stewart et al., 2019). Simulations are compared after 1000 years of spin-up from World Ocean Atlas 2013 (WOA13, Locarnini et al., 2013; Zweng et al., 2013) initial conditions. More information on ACCESS-OM2 including details on numerical algorithms, parameterizations and parameter choices is contained elsewhere (e.g. Holmes et al., 2021; Kiss et al., 2020; Stewart et al., 2017).

In ACCESS-OM2 the GM eddy transport parameterization is implemented via skew-diffusion (Griffies, 1998). The κ_{GM} structure, not altered in this study, is uniform in the vertical and dynamically dependent on the horizontal buoyancy gradient averaged over the top 2000 m according to the "baroclinic zone" setting (see Griffies, 2012; Griffies et al., 2005, Fig. 1b) with a maximum (minimum) of 600 $\mathrm{m^2\ s^{-1}}$ (50 $\mathrm{m^2\ s^{-1}}$).

In the default version of ACCESS-OM2 the neutral diffusivity κ_n is constant at 600 m^2 s^{-1}. This is altered for our experiments (see Section 2.3). To avoid unphysically large tracer fluxes the diffusive flux tapering method of Danabasoglu and McWilliams (1995) is used such that the fluxes are tapered where the neutral slope is large. This method avoids the potential for large spurious diapycnal fluxes that comes with alternative slope clipping methods. In ACCESS-OM2 the neutral diffusion operator is reduced to horizontal diffusion in the top surface layer (of thickness $\sim$ 2m) and bottom topography grid cells (Ferrari et al., 2008), meaning that the neutral diffusion parameterization can directly drive some diapycnal flux there, along with interactions with surface boundary layer turbulence and surface fluxes (de Lavergne, Groeskamp, Zika, & Johnson, 2022). We also note that model implementations of rotated neutral diffusion are affected by various numerical discretization errors that can create spurious diapycnal fluxes that are non-trivial to quantify and are treated elsewhere (e.g. Beckers et al., 1998, 2000; Griffies et al., 1998; Groeskamp et al., 2019; Lemarié et al., 2012; Shao et al., 2020; Urakawa et al., 2020).

2.2 A physics-based theory for the spatial structure of the neutral diffusivity

We follow Groeskamp et al. (2020) by building up physically-motivated three-dimensional maps of κ_n based on the following elements.

Two-dimensional mixing length theory (MLT)

Mixing-length theory (Prandtl, 1925) provides a two-dimensional structure for surface eddy-driven horizontal diffusion,

$$\kappa_{MLT}(x, y) = \Gamma\, u_{rms}\, L_{mix}, \tag{1}$$

where Γ is a mixing efficiency (here taken as 0.35, Klocker & Abernathey, 2013), u_{rms} is an RMS geostrophic velocity taken from altimetry observations and L_{mix} is a mixing length taken here as the deformation radius, L_d, associated with the first "surface mode" (LaCasce, 2017; LaCasce & Groeskamp, 2020), including an equatorial adjustment following Hallberg (2013).

Surface mode theory

A three-dimensional map can be obtained by assuming that u_{rms} follows the vertical structure of the first surface mode (LaCasce, 2017),

$$u_{rms}(x, y, z) = \phi(x, y, z)\sqrt{2EKE_0(x, y)}, \tag{2}$$

where $\phi(x, y, z)$ is obtained by solving the Sturm-Liouville problem dependent on the stratification profile at each horizontal location assuming that the horizontal velocity is zero at the bottom.

Mixing suppression by mean flows

We also include a factor that accounts for the suppression of neutral diffusion by mean flows following the theory of Ferrari and Nikurashin (2010). This factor has the form,

$$S(x, y, z) = \frac{1}{1 + k^2\gamma^{-2}(c_w - U)^2}, \tag{3}$$

where γ is an eddy time-scale (here a tunable parameter set to $\gamma^{-1} = 1.68$ days following Groeskamp et al. (2020)'s fit to NATRE and DIMES data), k is the zonal eddy wavenumber, c_w is an eddy drift speed and U is the mean velocity. k and c_w are determined according to surface mode theory, while U here comes from the thermal wind relation applied to climatological ocean observations (note that a reference level velocity is not needed, Groeskamp et al., 2020).

Table 1. List of ACCESS-OM2 experiments

Experiment	Description	Volume-mean κ_n (m^2 s^{-1})	Surface-mean κ_n (m^2 s^{-1})
CTRL	600 m^2 s^{-1} maximum	373	385
HIGH	1200 m^2 s^{-1} maximum	747	770
LOW	100 m^2 s^{-1} maximum	64	62
MLT2D	Mixing-length theory	1808	1693
MLT3D	MLT2D + vertical modes	473	1693
FULL	MLT3D + suppression	222	503

Grid-scaling factor

As even coarse-resolution models can resolve some eddy activity in the tropics where the associated length scales are larger, we also include a grid-scaling factor, not considered by Groeskamp et al. (2020), that reduces κ_n where eddy-mixing may be resolved following Hallberg (2013),

$$g(x, y) = \frac{\Delta^2}{\Delta^2 + L_d^2}, \tag{4}$$

where Δ is a measure of the grid spacing, taken as the harmonic mean of the zonal and meridional grid spacings,

$$\Delta = \frac{2\Delta x \Delta y}{\Delta x + \Delta y}, \tag{5}$$

and we take the surface mode deformation radius (LaCasce, 2017) rather than the standard first-baroclinic deformation radius for L_d in Eq. (4). We also set a minimum on κ_n of 20 m^2 s^{-1} (following Adcroft et al., 2019).

2.3 Experiments

The experiments considered in this study are listed in Table 1. Our control experiment (CTRL) is identical to the ACCESS-OM2 default configuration except that it includes the grid-scaling factor [Eq. (4)] which reduces κ_n near the Equator (Fig. 1a). This grid-scaling reduction near the equator has negligible impact on the simulations relative to the differences between the other experiments described below.

CTRL will be compared to five other experiments. All experiments include the grid-scaling factor [Eq. (4)]. HIGH and LOW are scaled versions of CTRL with a maximum coefficient of 1200 m^2 s^{-1} (HIGH) or 100 m^2 s^{-1} (LOW). Experiment MLT2D introduces horizontal variations in κ_n through mixing length theory [Eq. (1)]. MLT2D has a significantly larger κ_n throughout the tropics and mid-latitudes compared to CTRL with decreases only in the very high-latitudes (Fig. 2a). Experiment MLT3D then adds the vertical modal structure [Eq. (2)] which results in a decay of κ_n with depth (Fig. 2b). Finally FULL adds the effects of mixing suppression by mean flows [Eq. (3)]. This factor significantly reduces κ_n throughout the domain (compare Figs. 2a,b with 2c,d, the surface mean κ_n is reduced by more than a factor of 3, Table 1). Compared to CTRL, FULL is characterized by higher values in the shallow mid-latitudes and lower values in the high-latitudes and at depth (Fig. 2d). The mean flow suppression factor can also result in subsurface maximum's in κ_n, notably in the ACC region (Fig. 2d) where subsurface critical layers form as the mean flow speed decays in the vertical, consistent with theory and diagnostics from high-resolution idealized models (e.g. Abernathey et al., 2013, 2010; Ferrari & Nikurashin, 2010; Smith & Marshall, 2009).

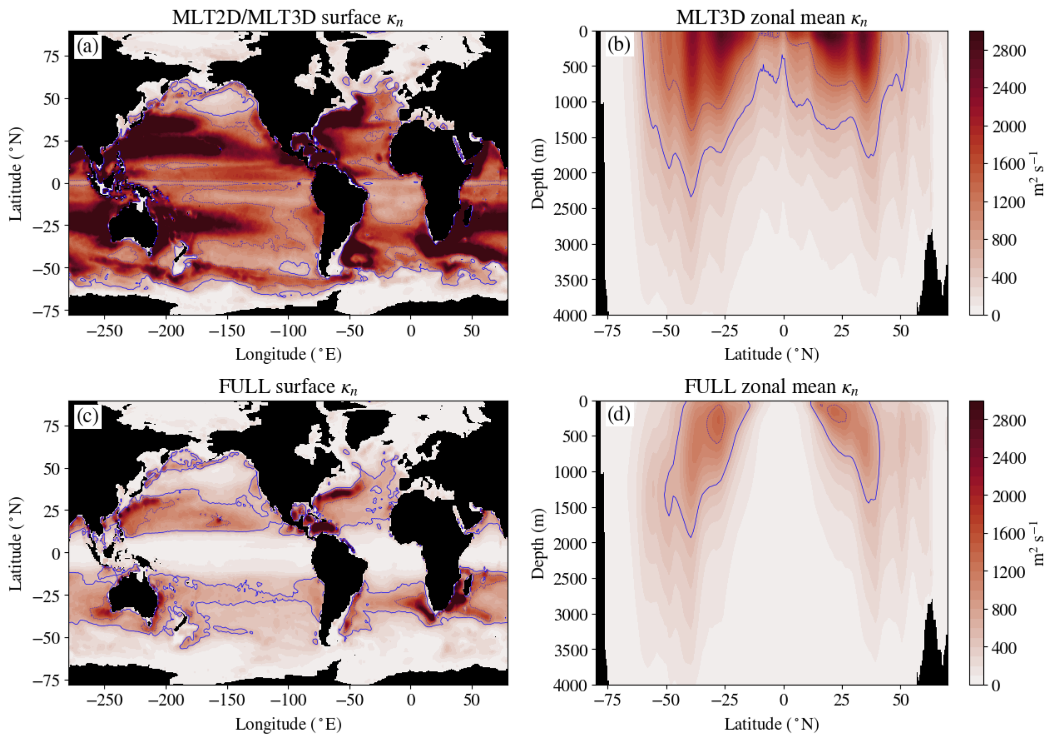

Figure 2. (a,c) Surface κ_n and (b,d) zonal mean κ_n for experiments (a,b) MLT3D (c,d) FULL. The thick (thin) blue contours indicate the 600 m^2 s^{-1} (1200 m^2 s^{-1}) isosurfaces.

3 Results

We begin by describing the temporal behavior of the solutions over the 1000 year spin-up period (Section 3.1) and the observed changes in the ocean's zonal-mean overturning circulation (Section 3.2), meridional heat transport (3.3) and tracer fields (Section 3.4). The mechanisms linking the neutral diffusivity to changes in the interhemispheric overturning cell are then explored in Sections 3.5-3.8. Section 3.9 discusses the Antarctic bottom water cell.

3.1 Scalar variables and model spin-up

In order to allow for the slow adjustment of the deep ocean all experiments have been spun-up for 1000 years (Fig. 3). The choice of κ_n has a strong impact on the drift in global ocean heat content (compare solid lines in Fig. 3a). The evolution of global ocean heat content is determined by the net air-sea heat flux, which depends through the bulk formula on the sea surface temperature (SST). Indeed, those experiments with generally smaller values of κ_n have cooler global-mean SST in the first few 100 years that drives a positive drift in ocean heat content (e.g. experiment LOW, green lines in Fig. 3a,b). In contrast, larger values of κ_n correspond to warmer transient SSTs and net ocean heat loss (e.g. experiment HIGH, orange lines in Fig. 3a,b). However, the structure in κ_n also impacts the SST and ocean heat content trends; SST is warmest in experiments MLT2D and MLT3D which may be because of the strong neutral diffusion in the Western Boundary Current regions (e.g. Fig. 2a).

The choice of κ_n also has an impact on both the interhemispheric (alternatively "deep", "upper", or North Atlantic Deep Water, NADW) and Antarctic bottom water

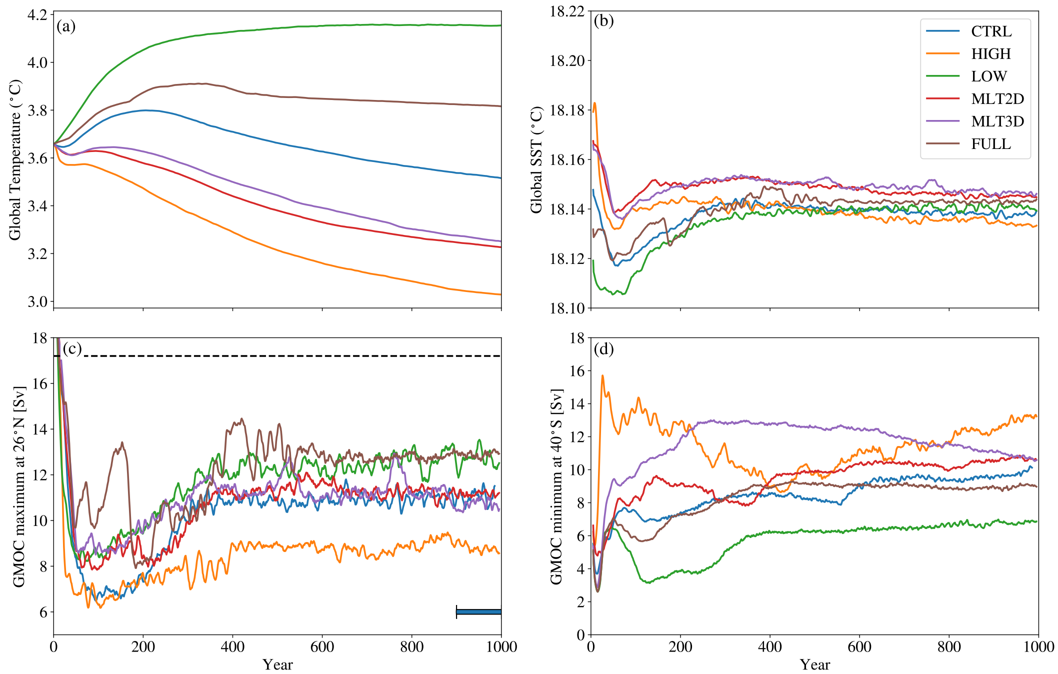

Figure 3. Time series of (a) global average Conservative Temperature (°C), (b) global average SST (°C), (c) the maximum of the global MOC in potential density (referenced to 2000 dbar, σ_2) at 26°N (Sv), a proxy for the strength of the interhemispheric overturning cell and (d) the minimum of the global σ_2 MOC at 40°S (Sv), a proxy for the strength of the bottom water cell from all experiments. The dashed black line in panel c indicates the observational value of 17.2 Sv from the RAPID array in the Atlantic (McCarthy et al., 2015). A 10-year running mean smoothing has been applied to panels b-d. The blue bar in panel c indicates the averaging period used for most comparative diagnostics in later figures.

cells of the zonally-integrated MOC in potential density coordinates (Fig. 3c,d). The deep cell achieves equilibrium after $\sim$ 600 years, while the bottom water cell is still trending after 1000 years. In the remainder of the article we focus on differences in the circulation and tracer structure averaged over the last 100 years (blue bar in Fig. 3c).

3.2 The meridional overturning circulation

Stronger (weaker) neutral diffusion drives a broad weakening (strengthening) of the interhemispheric overturning cell (blue in HIGH, Fig. 4c and red in LOW, Fig. 4e). These changes in the deep cell are dominated by the Atlantic basin (not shown) as part of the Atlantic MOC (AMOC). Accompanying these changes in the magnitude of the overturning are shifts in the density of the NADW outflow, which becomes denser when κ_n is increased in HIGH (red patch below $\sigma_2 = 1036.5$ kg m^{-3} in the Northern Hemisphere in Fig. 4c) and less dense in LOW (Fig. 4e). These changes in NADW density may be a consistent response to the change in the strength of the AMOC, in these quasi-equilibrated simulations where the interior density field has had sufficient time to adjust. A weaker AMOC reduces the input of warm surface water into the North Atlantic (see Section 3.3), leading to SST cooling, reduced surface heat loss, and reduced NADW formation while the NADW that is formed is denser. Likewise, with increased input of warm surface water into the North Atlantic under an enhanced AMOC, there is more surface heat loss leading to more NADW formation but at lighter density classes. The shift in NADW outflow density are also consistent with the entire ocean being denser (lighter) and less (more) stratified in HIGH (LOW), as will be discussed in more detail in Section 3.4.

Change in the bottom water cell mirror those in the interhemispheric cell. The bottom water cell is stronger in HIGH and weaker in LOW (Fig. 4c,e below $\sigma_2 = 1036.9$, also see Fig. 3d). However, these changes are less linear than for the interhemispheric cell; with a strong shut down in LOW compared to a weak strengthening in HIGH. This asymmetry may be partially explained by the overlap in density between the denser NADW outflow in HIGH and the bottom-cell.

Adding spatial structure to κ_n in the MLT2D, MLT3D and FULL experiments has additional impacts. Experiments MLT2D and MLT3D, both corresponding to an increase in the global average κ_n compared to CTRL (see Table 1), show a similar pattern of anomalous overturning to HIGH, albeit with weaker anomalies (compare Figs. 4g,i with Fig. 4c). The weaker MOC anomalies in MLT2D compared to HIGH, despite MLT2D having a larger surface- and volume-mean κ_n (see Table 1), highlights the importance of the horizontal structure of κ_n. In particular, it suggests that the smaller or similar κ_n at high-latitudes in MLT2D (compared to CTRL or HIGH) are more important than the much larger values at mid-latitudes (Fig. 2a). MLT2D and MLT3D are similar, suggesting that the vertical structure of κ_n has only a minor impact on the MOC. Compared to CTRL, MLT2D and MLT3D are characterized more by a shift in the peak density of the interhemispheric cell rather than a change in strength (compare red and purple with blue lines in Figs. 5a,b).

The weakening of κ_n through mean-flow suppression introduced in FULL has a significant impact on the MOC, with a similar pattern of MOC anomalies to LOW (Fig. 4k). The interhemispheric cell responses in FULL and LOW are both around 2 Sv (a $10-20\%$ change from CTRL), although in FULL there is a smaller shift in the density of the maximum overturning (compare green and brown with blue lines in Fig. 5a,b). While the purpose of this study is not to better tune the model, it should be noted that ACCESS-OM2 has a weak interhemispheric cell compared to observations (compare solid lines to dashed RAPID estimate in Fig. 3a), a comparison that is improved in FULL and LOW (note that the cell is better represented in the $1/4^\circ$ and $1/10^\circ$ configurations of ACCESS-OM2, Kiss et al., 2020). While this suggests that κ_n may be too large in ACCESS-OM2, the structure in κ_n is also clearly important. While LOW results in a strong, consistent weakening of the likely already too weak bottom water cell (Kiss et al., 2020), FULL has a negligible impact on the bottom water cell (Figs. 4e,k, 3d). Changes in the bottom water cell are discussed further in Section 3.9.

3.3 Meridional heat transport

The ocean's meridional heat transport (MHT) is influenced by κ_n both directly, from changes in the diffusive component of MHT, and indirectly due to circulation (e.g. MOC) changes. The diffusive component of MHT (dashed lines in Fig. 6) is only significant in CTRL in the Southern Ocean south of $\sim 40°$S, where its sensitivity to κ_n dominates the changes in total MHT (compare solid and dashed lines in Fig. 6b). The weak change in the advective/circulation component of MHT in the Southern Ocean contrasts with results from coupled models where wind changes are permitted and compensation between diffusive and advective heat transport can occur (e.g. Pradal & Gnanadesikan, 2014). North of $\sim 40°$S changes in total MHT are largely driven by the changes in the AMOC discussed above (Fig. 6d). In FULL, the change in the MHT in the Atlantic is about 0.05PW, corresponding to $8-17\%$ of the CTRL MHT in the Atlantic. In the HIGH and LOW experiments there are also some small changes in the South Pacific and Indian Oceans, which are largely absent in FULL (Fig. 6c). This is linked to the lack of change in the bottom water cell in FULL. The bottom water cell anomalies

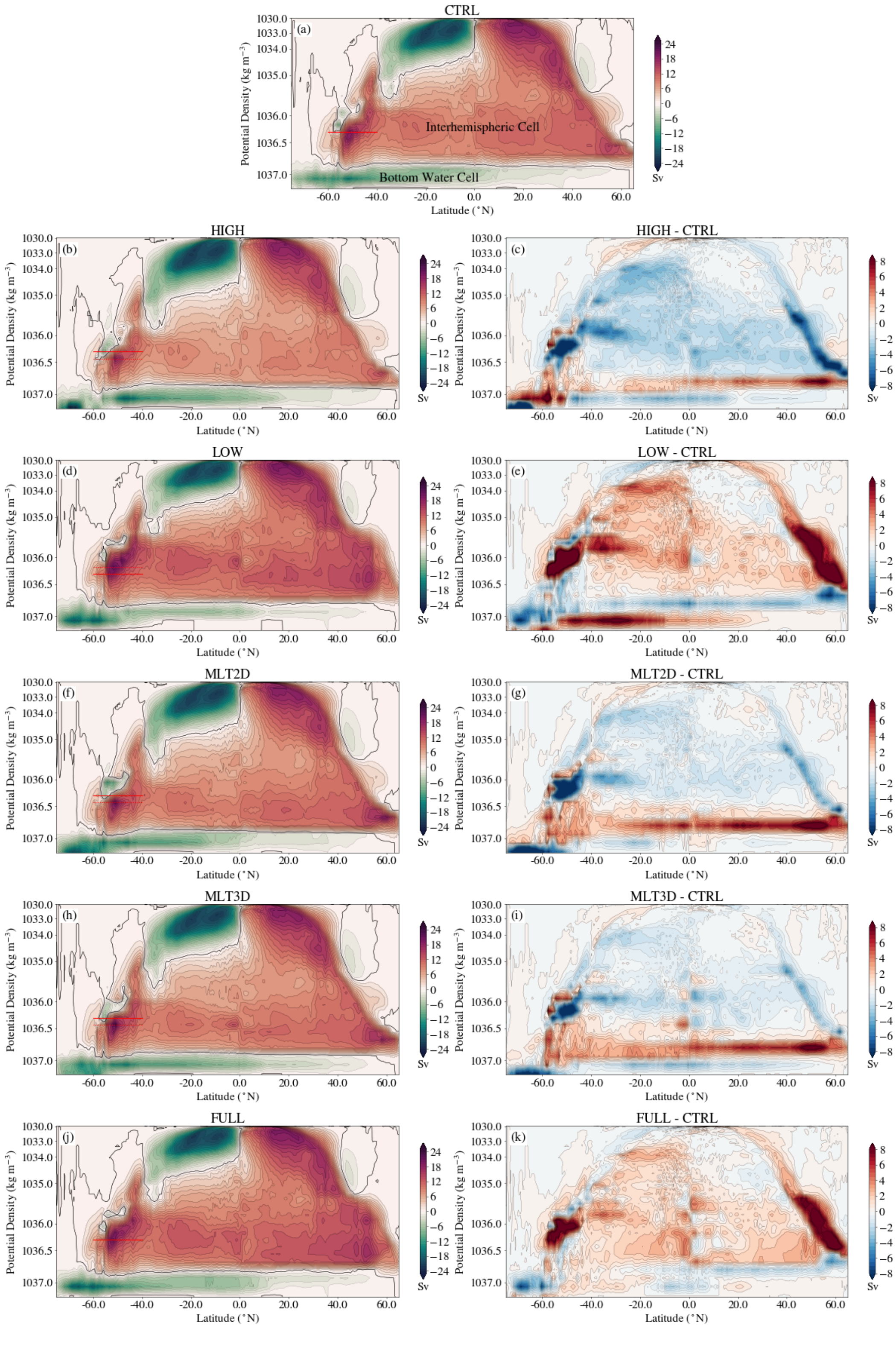

Figure 4. Global MOC in potential density (referenced to 2000 dbar) σ_2-latitude coordinates for the (a) CTRL, (b) HIGH, (d), LOW, (f) MLT2D, (h) MLT3D and (j) FULL experiments. The σ_2 density bin sizes are 0.125kgm^{-3}. Red (green) colors indicate clockwise (anti-clockwise) circulation. The panels on the right show the difference between each run and the CTRL experiment, with red (blue) colors indicating anomalous clockwise (anti-clockwise) circulation. Thus red (blue) colors indicate a strengthening of the interhemispheric (bottom water) cells, labeled in panel a, and vice versa. The red solid line in each panel marks $\sigma_2 = 1036.3125$, the density of the maximum overturning streamfunction in the Southern Ocean in CTRL (panel a). The dashed red lines in panels b,d,f,h and j indicate the equivalent maximum overturning density in each

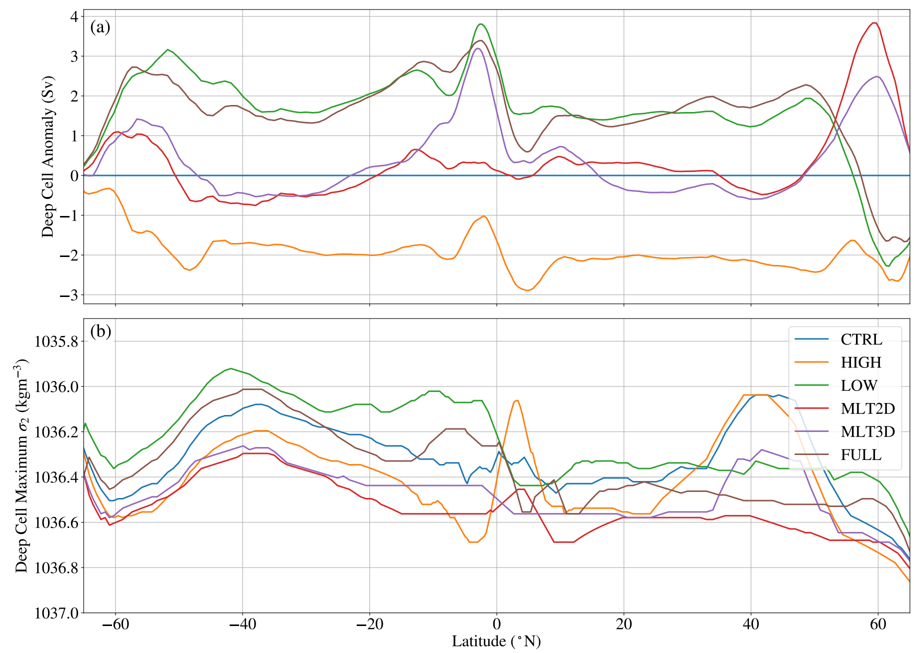

Figure 5. (a) Anomaly in the maximum transport of the interhemispheric cell, defined as the maximum value of the σ_2 overturning streamfunction at densities denser than 1035.6 kg m^{-3}, and (b) the corresponding density as a function of latitude. All curves have been smoothed using a 15-point moving average filter in latitude.

dominate the Indo-Pacific density-space overturning differences between LOW and FULL (compare Fig. 4e,k).

3.4 Zonal mean tracer fields

The changes in κ_n have an impact on zonal mean temperature and salinity biases (Fig. 7). CTRL has a warm and salty bias reaching 1.5°C and 0.3 psu in the upper 1000 m north of 60°S and a cold/fresh bias south of 60°S and below 2500 m depth when compared to observations (Figs. 7e,f). Compared to CTRL, HIGH shows large-scale cooling of the ocean below the top 500m, a saltier upper ocean and reduced ideal age throughout most of the interior (indicating increased ventilation, Fig. 7h-j, England & Rahmstorf, 1999; Jones & Abernathey, 2019). The bulk cooling with increased κ_n is consistent with Danabasoglu and McWilliams (1995) who found similar results when varying κ_n and κ_{GM} in tandem. Changes in LOW are largely opposite to HIGH and are consistent with an increase in the interhemispheric cell, although the anomalies are somewhat stronger in LOW than HIGH with warming in the Southern Ocean reaching 1.5°C (Fig. 7l-n).

Adding spatial structure to κ_n further alters the hydrography. The surface-intensified increase in κ_n in MLT3D drives cooling and increased ventilation (with some surface-intensified salinification) that is focused in the upper ocean compared to HIGH (compare Figs. 7h,p,i,q,j,k). FULL shows anomalies that are similar to LOW as κ_n is reduced in most locations (Fig. 7s). However, FULL is cooler than LOW (and CTRL) in the upper 1000 m in the mid-latitudes and tropics (Fig. 7t). Encouragingly, the warming/salinification in the deep ocean and high latitudes, and the cooling/freshening above 1000 m, in FULL largely opposes the CTRL WOA13 biases (compare Figs. 7t,k to Figs. 7e,f), meaning that these biases are reduced in FULL.

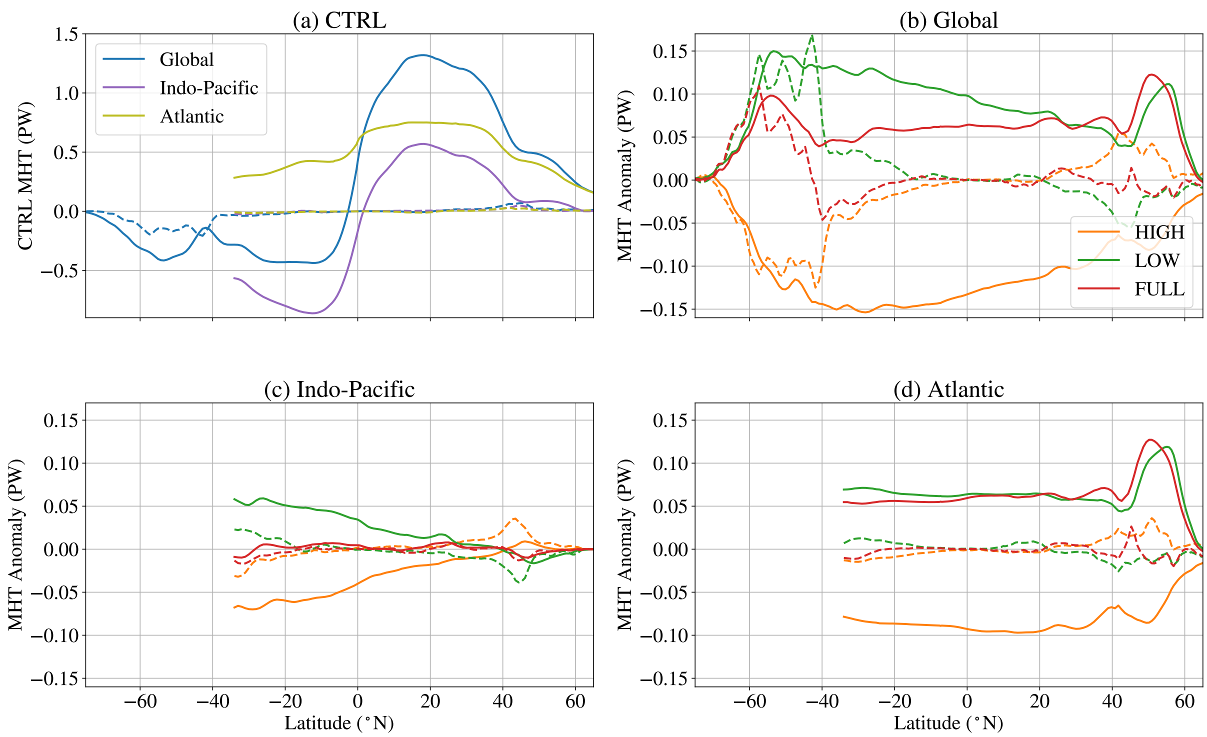

Figure 6. Meridional heat transport (MHT, PW) in (a) CTRL and MHT anomalies for the (b) global ocean, the (c) Indo-Pacific and the (d) Atlantic basins in HIGH, LOW and FULL. The solid lines show the total MHT and the dashed lines show the component due to neutral diffusion.

3.5 Where do changes in neutral mixing have an impact?

We now turn to the mechanisms that link the circulation and tracer anomalies discussed above to the structure of κ_n. While κ_{GM} directly affects the residual overturning circulation and isopycnal slopes, particularly in the Southern Ocean and in deep-water formation regions (e.g. Döös & Webb, 1994; England & Rahmstorf, 1999; Gent, 2011), the impact of κ_n on circulation is less obvious as neutral diffusion does not have a *direct* impact on the ocean's density field. Instead, κ_n impacts the circulation indirectly by altering the surface buoyancy forcing and through non-linear equation of state effects such as cabbeling (Klocker & McDougall, 2010) as will be discussed in Sections 3.6 and 3.7 respectively. These impacts are strongest where along-isopycnal temperature and salinity gradients strongest; in the Southern Ocean between 40°S and 60°S and in the North Atlantic (Fig. 8a,b, also see Fig. 6a). In both these regions there is a distinct pattern of cold and fresh surface waters and warm and salty interior waters following isopycnals (Fig. 8a, Fig. 7b,c), due to net precipitation and sea ice melt at high-latitudes. Thus, increases in κ_n (e.g. in HIGH) have their largest impacts here, where surface-intensified salinification and depth-intensified cooling (compared to CTRL) reflect a reduction in the along-isopycnal temperature and salinity gradients (Fig. 7h,i). In contrast, decreasing κ_n in LOW leads to weak surface cooling, strong surface freshening and salinification/warming at depth (Fig. 7,l,m). SST changes are weaker than temperature changes at depth because they are damped by surface flux responses.

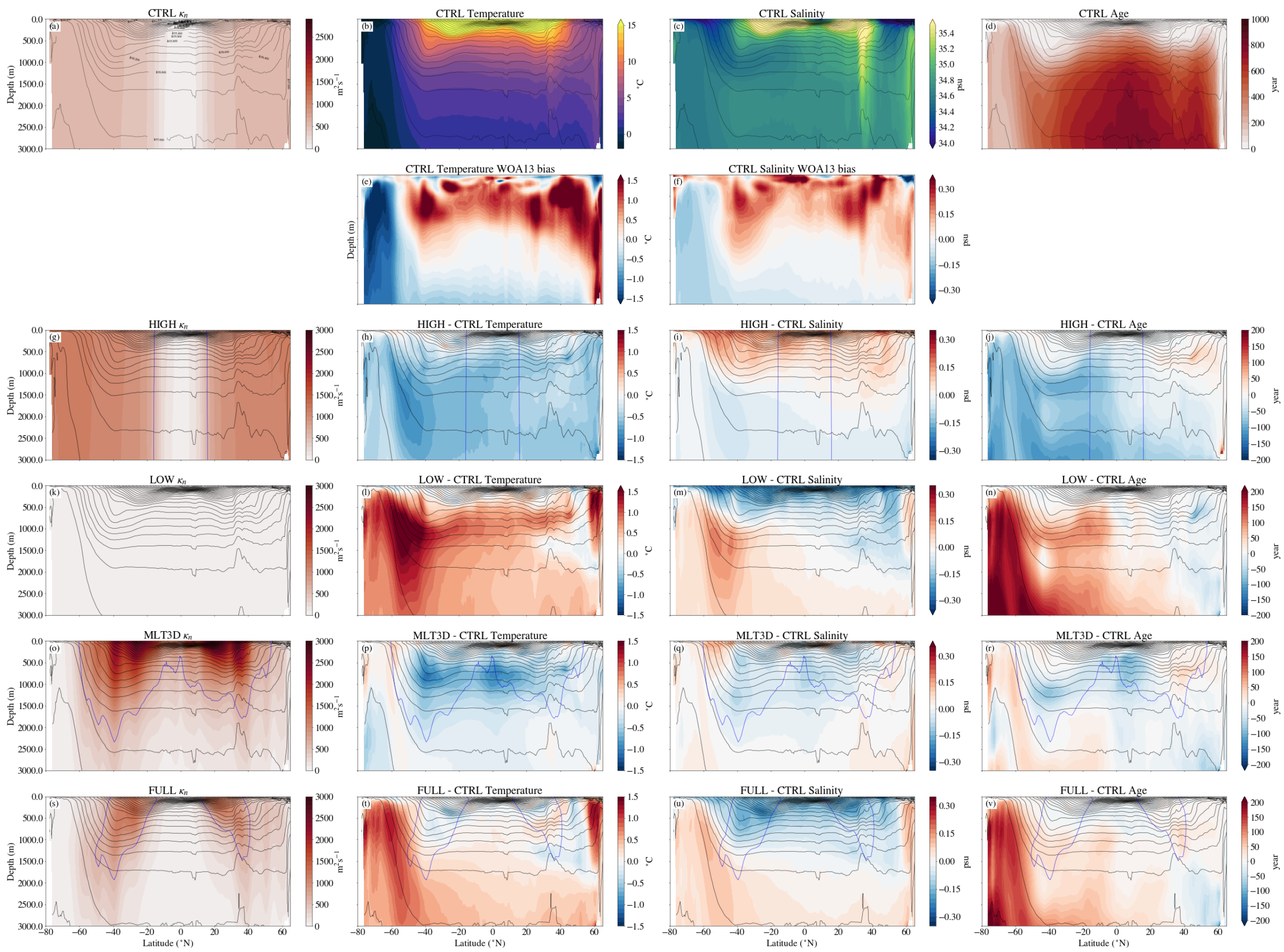

Figure 7. Zonal-mean (a,g,k,o,s) κ_n and (h,l,p,t) temperature, (i,m,q,u) salinity and (j,n,f,v) ideal age anomalies compared to the CTRL experiment (b,c,d) for experiments (g-j) HIGH, (k-n) LOW, (o-r) MLT3D and (s-v) FULL. MLT2D (not shown) has similar temperature and salinity anomalies to MLT3D. (e) Temperature and (f) salinity biases of CTRL relative to WOA13. The black contours represent σ_2 potential density contours at 0.1 kg m^{-3} spacing. The thin blue contours in panels g-v indicate the 600 m^2 s^{-1} κ_n isosurface.

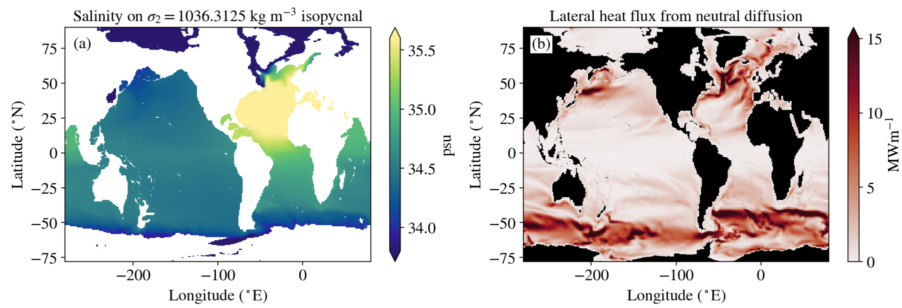

Figure 8. (a) Salinity on the $\sigma_2 = 1036.3125$ kg m^{-3} isopycnal and (b) the magnitude of the vertically-integrated lateral heat flux due to neutral diffusion in CTRL. Along-isopycnal salinity gradients are strongest at high-latitudes. As κ_n is constant outside the equatorial region in CTRL, the heat flux in panel b indicates the presence of strong instantaneous along-isopycnal temperature and salinity gradients throughout the water-column, where changes in κ_n would be expected to have their largest impact.

3.6 The surface flux response to κ_n

Changes in SST induced by changes in κ_n impact the surface heat and freshwater fluxes through the bulk formula (Large & Yeager, 2004, additional feedbacks would play a role in a coupled model). In the zonal mean, changes in SST are strongest in the Southern Ocean around and just north of 60°S and in the North Atlantic north of 40°N (Fig. 9a). SST changes in the tropics and mid-latitudes are minimal. The surface cooling in the Southern Ocean when κ_n is reduced (LOW, orange lines in Fig. 9) induces an anomalous heat flux into the ocean at these latitudes through the bulk formula (Q_H, Fig. 9c). North of $\sim$ 64°S the cooling also reduces evaporation, resulting in an increase in the net surface volume flux into the ocean (P-E+R+I, Fig. 9d). Thus, changes in both surface heat and volume fluxes in response to the (initially compensated) SST anomalies lead to an anomalous buoyancy flux *into the ocean* when SST is cooled (LOW and FULL, orange and green lines in Fig. 9e) and an anomalous buoyancy flux *out of the ocean* when SST is warmed (HIGH, blue line in Fig. 9e).

The above physical interpretation for the changes in buoyancy flux holds outside of the region of permanent influence of sea ice (north of $\sim$ 65°S in the Southern Hemisphere, Fig. 9g). South of 65°S in HIGH there is instead an increase in the surface volume flux into the ocean associated with enhanced sea-ice melt driven by the increased upward neutral-diffusive heat flux (blue line in Fig. 9d). However, in these experiments the changes in sea-ice cover are relatively minor (Fig. 9g, being restricted to movements of the seasonal maximum sea-ice edge of a maximum of a few degrees latitude, not shown) and buoyancy flux anomalies in the sea-ice affected region are weaker than further northward (Fig. 9e). Note that the relatively minor role of sea-ice changes here contrasts with studies performed in coupled models where atmosphere-ocean-sea ice feedbacks can amplify the response to changes in neutral diffusion (e.g. Pradal & Gnanadesikan, 2014).

Surface property and flux anomalies are large and variable in the North Atlantic, reflecting the strong direct impact of AMOC changes. Surface heat and buoyancy flux anomalies north of 45°N are as large as the weak CTRL heat and buoyancy fluxes in these regions (not shown). Below we will argue that AMOC changes (and their subsequent impacts on surface flux anomalies in the North Atlantic) are driven by the changes in the Southern Ocean.

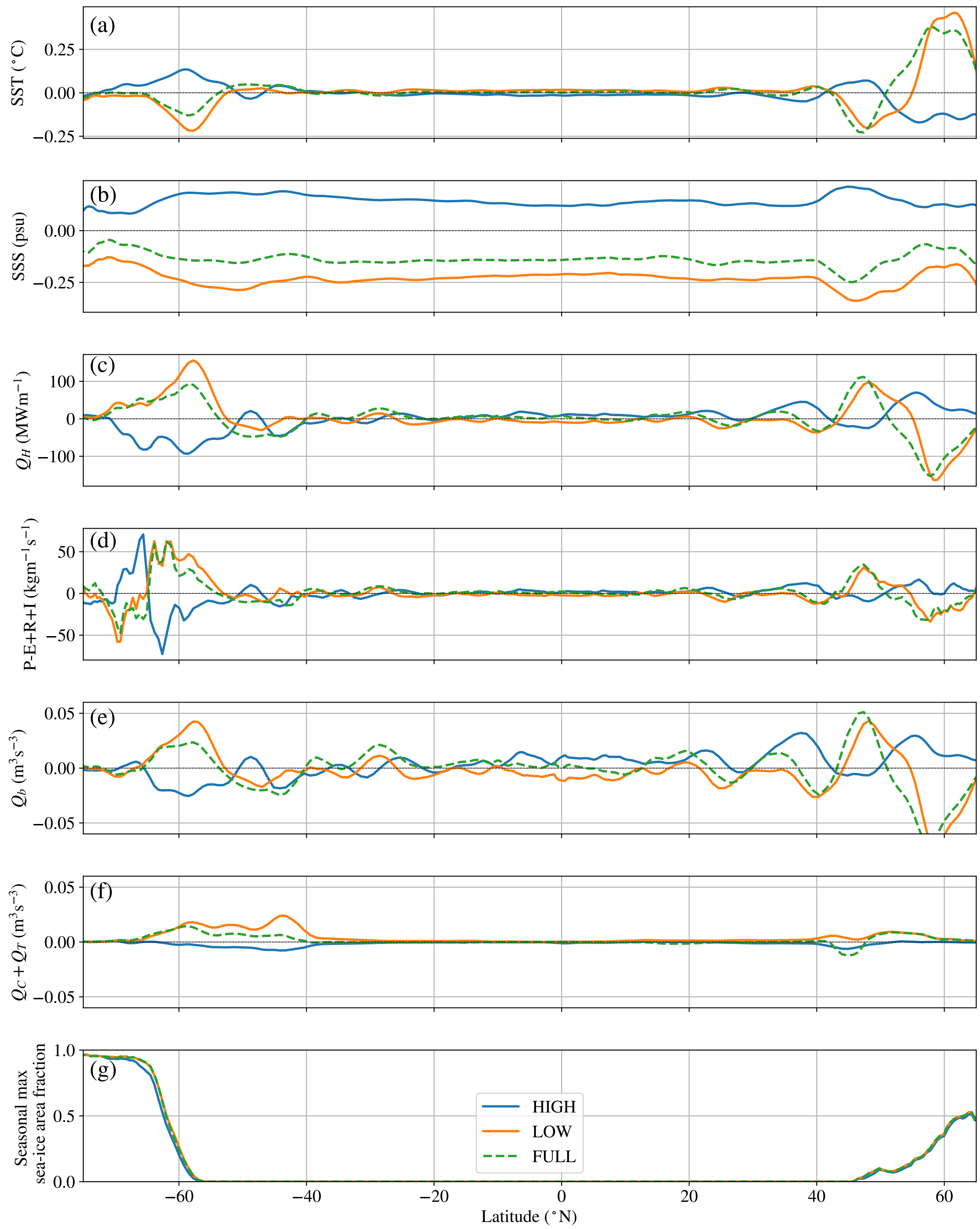

Figure 9. Anomalies compared to CTRL in zonal-mean (a) SST, (b) SSS and zonal total (c) surface heat (Q_H), (d) surface volume (including precipitation, evaporation, river runoff and ice-ocean volume exchanges, P-E+R+I), (e) surface buoyancy (Q_B) and (f) vertically-integrated cabbeling and thermobaricity buoyancy flux convergence anomalies in the HIGH (blue), LOW (orange) and FULL (green dashed) experiments. The fluxes in panels c-f are positive when into the ocean (i.e. a positive Q_b indicates a lightening of surface waters). Each curve has been smoothed using a 5-point latitude smoother for display purposes. (g) The seasonal maximum of the zonal mean sea ice-area fraction.

Changes in κ_n also impact the zonal mean sea surface salinity (SSS) which freshens (becomes saltier) when κ_n is decreased (increased, Fig. 9b). These SSS anomalies are relatively uniform across the whole globe and reflect the increased export of freshwater northward out of the Southern Ocean when the interhemispheric overturning cell is enhanced.

The buoyancy flux anomalies between $\sim 65°$S and 55°S (Fig. 9e) that result from the SST anomalies, drive a modification in surface flux-driven watermass transformation. When κ_n is reduced the resulting positive anomalous buoyancy flux into the ocean (LOW and FULL in Fig. 9e) drives an anomalous cold-to-warm or dense-to-light watermass transformation. This response, which is at equilibrium, suggests that more upwelled water is being converted to lighter waters and moving northward as part of the interhemispheric overturning cell, rather than being converted to denser waters and participating in the bottom water cell. The changes in buoyancy fluxes are therefore consistent with an enhanced interhemispheric overturning cell. In contrast, when κ_n is increased the anomalous buoyancy flux is out of the ocean (HIGH in Fig. 9e) and thus surface-driven "diapycnal upwelling" is reduced at these latitudes, consistent with a reduced interhemispheric overturning cell. It is important to note that these are quasi-equilibrium anomalies. The SST anomalies induced by the changes in κ_n are initially compensated. The surface buoyancy flux response to these initial anomalies first acts to change the surface and interior buoyancy field (as described in Section 3.8) before settling into this new equilibrium. However, these surface buoyancy flux driven watermass transformation changes are also reinforced by changes in watermass transformation associated with cabbeling and thermobaricity.

3.7 Cabbeling and thermobaricity

Changes in κ_n can also lead directly to changes in the interior buoyancy structure (and thus circulation), though non-linear equation of state effects. Straightforward manipulation of the neutral diffusion source term on the RHS of the material time derivative for locally referenced potential density $D\rho/Dt$ (e.g. see Section 36 of Griffies, 2012) yields,

$$-\rho_0\alpha\nabla\cdot\mathbf{J}^{\Theta} + \rho_0\beta\nabla\cdot\mathbf{J}^{S} = \kappa_n\rho_0\left(C|\nabla_n\Theta|^2 + T\nabla_n P\cdot\nabla_n\Theta\right), \tag{6}$$

where ρ is locally referenced potential density, Θ is Conservative Temperature (McDougall, 2003; McDougall & Barker, 2011), S is salinity (ACCESS-OM2 ostensibly uses practical salinity as its prognostic salt variable and the Jackett et al., 2006, pre-TEOS10 equation of state), α and β are the thermal expansion and haline contraction coefficients, $\mathbf{J}^{\Theta}$ and $\mathbf{J}^{S}$ are the neutral diffusive fluxes of Θ and S, ∇_n represents the two-dimensional horizontal gradient operator along neutral directions, P is pressure and,

$$C = \frac{\partial\alpha}{\partial\Theta} + 2\frac{\alpha}{\beta}\frac{\partial\alpha}{\partial S} - \left(\frac{\alpha}{\beta}\right)^2\frac{\partial\beta}{\partial S}, \tag{7}$$

$$T = \frac{\partial\alpha}{\partial P} - \frac{\alpha}{\beta}\frac{\partial\beta}{\partial P}. \tag{8}$$

While the neutral diffusive fluxes $\mathbf{J}^{\Theta}$ and $\mathbf{J}^{S}$ are directed along neutral tangent planes by construction, the dependence of α and β on temperature and salinity [*cabbeling*, Eq (7)] and pressure [*themobaricity*, Eq. (8)] can result in a material source of density and thus a diapycnal volume flux (Groeskamp et al., 2016; Klocker & McDougall, 2010; McDougall, 1987; Nycander et al., 2015). Here we quantify cabbeling and thermobaricity as buoyancy flux convergences using Eq. (6), consistent with the numerical discretization of the neutral fluxes themselves as described in more detail in Chapter 36 of Griffies (2012).

In CTRL, cabbeling acts as a sink of zonally-integrated buoyancy in the high-latitude regions where along-isopycnal temperature gradients are largest (Fig. 10a). Cabbeling

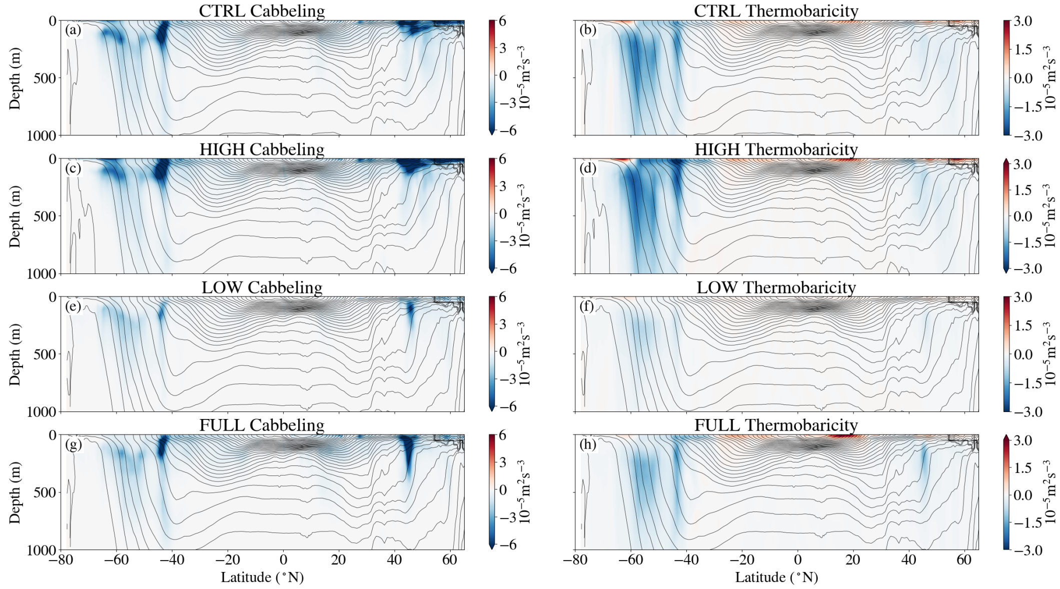

Figure 10. Zonal sum of the buoyancy flux convergence due to (a,c,e,g) cabbeling and (b,d,f,h) thermobaricity quantified using Eq. (6) (converted to buoyancy by multiplying by $-g/\rho_0$) in the CTRL, HIGH, LOW and FULL experiments. Note that the thermobaricity color scale is one half that of the cabbeling scale.

has been shown to be important for the formation of Antarctic Intermediate Water (e.g. Nycander et al., 2015). Thermobaricity has a smaller impact as a sink of buoyancy throughout the Southern Ocean interior as well as a source in isolated regions near the surface (Fig. 10b, note the color-scale difference between Figs. 10a,b). When κ_n is increased (decreased) in HIGH (LOW/FULL), cabbeling and thermobaricity are increased (decreased) with little change in pattern. Thus, in the LOW and FULL experiments, we expect a decrease in the magnitude of light-to-dense watermass transformation, or an anomalous *dense-to-light transformation*, due to non-linear equation of state effects in these regions.

Vertically integrating the anomalous cabbeling and thermobaricity flux convergences allows the associated transformation to be compared quantitatively to the surface-driven transformation anomalies in a bulk sense (compare Figs. 9e,f). Between 65°S and 50°S where the surface buoyancy flux anomalies are largest, the reduction in cabbeling and thermobaricity in LOW and FULL corresponds to an effective positive buoyancy flux anomaly of 30−50% the size of the surface buoyancy flux anomalies. Furthermore, there is also a significant reduction in cabbeling and thermobaricity in LOW and FULL futher north, up to 40°S. In contrast, changes in cabbeling and thermobaricity in the North Atlantic are much smaller than the changes in the surface buoyancy flux. The impact of these changes on the density field is examined next.

3.8 Impacts on interior density and circulation

The additional buoyancy fluxed into the ocean through the surface when κ_n is reduced in LOW is carried northwards in the downwelling arm of the Southern Ocean overturning circulation. Combined with reduced cabbeling and thermobaricity (e.g. Fig. 10e near 40°S), this leads to a broad lightening of the "bowl" of waters in the upper ~ 1000m in the tropics and mid-latitudes (Fig. 11f), a signal in density that is more coherent than in temperature or salinity (compare Figs. 11e,f). This bowl is approximately bound below by the σ_2 isopycnal corresponding to the maximum in the Southern Ocean overturn-

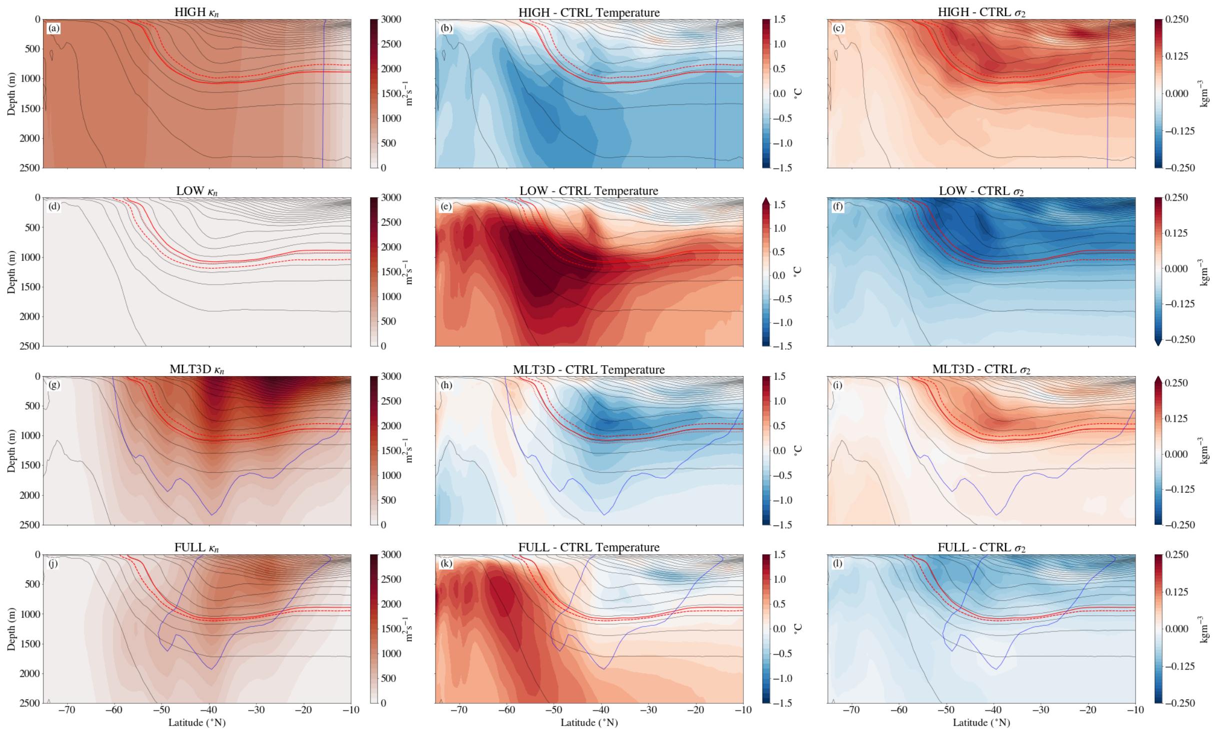

Figure 11. Zonal mean (a,d,g,j) κ_n, (b,c,h,k) temperature anomalies and (c,f,i,l) σ_2 potential density anomalies in (a,b,c) HIGH, (d,e,f) LOW, (g,h,i) MLT3D and (j,k,l) FULL in the Southern Hemisphere. The black contours show σ_2 at 0.1 kg m^{-3} intervals. The solid (dashed) red lines indicate the CTRL (HIGH/LOW/MLT3D/FULL) 1036.3125 kg m^{-3} σ_2 isopycnal, which corresponds to the maximum in the CTRL overturning streamfunction. The dotted red lines indicate the maximum overturning isopycnal in the perturbation experiments (see Fig. 5).

ing streamfunction (red lines in Fig. 11, as quantified from Fig. 5), which outcrops near the latitude of maximum wind stress separating Ekman-driven upwelling to the south from downwelling to the north (Stewart & Hogg, 2019; Stewart et al., 2021). In CTRL the maximum overturning is found on the $\sigma_2 = 1036.3125$ kg m^{-3} isopycnal (red solid lines in all panels of Fig. 11), which shifts either northward (in HIGH and MLT3D, dashed red lines in Figs. 11a,g) or southward (in LOW and FULL, Figs. 11d,j), consistent with the changes in transformation. As the surface winds are fixed in these experiments[1] this results in a shift in the projection of the wind stress onto the outcropping density field (Fig. 12). For example, in LOW the density marking both the zero wind stress curl (compare green and blue lines in Fig. 12) and the maximum in the Southern Ocean overturning streamfunction (compare dashed and dotted lines in Figs. 11d,e,f, or Figs. 4a,d) becomes lighter.

The coherent upper ocean density changes (Fig. 11c,f,i,l) illustrate that experiments with reduced κ_n have a stronger upper ocean stratification and vice versa. Stronger upper ocean stratification leads to an enhanced interhemispheric cell overturning through thermal wind balance (e.g. Wolfe & Cessi, 2010) and is consistent with the requirement that more overturning balances increased surface flux-driven, and decreased cabbeling

[1] note that the impact of changes in surface currents (through relative wind) and SST on the wind stress are less than 1%.

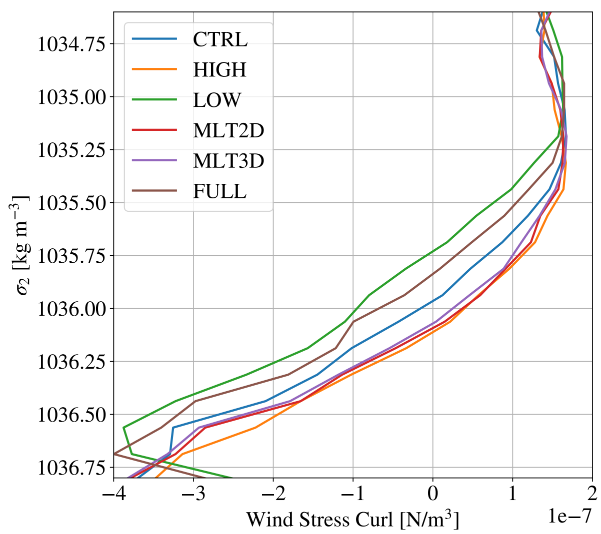

Figure 12. Wind stress curl binned into σ_2 coordinates using the annual mean surface σ_2 and wind stress fields. The isopycnal corresponding to the zero in the wind stress curl shifts toward lighter (denser) densities in the experiments where κ_n is decreased (increased). Note that the isopycnals associated with the zero wind-stress curl and those identified as marking the maximum in the Southern Ocean overturning streamfunction do not correspond exactly due to modification by surface flux- and mixing-driven watermass transformation.

and thermobaricity-driven, dense-to-light watermass transformation. This mechanism is illustrated in Fig. 13 and summarized in the caption.

The mechanism illustrated in Fig. 13 suggests that changes in the North Atlantic are slave to what happens in the Southern Ocean. Our results appear to be inconsistent with the alternative hypothesis that changes in κ_n in the North Atlantic are the main driver. An increase in κ_n in the North Atlantic would, like in the Southern Ocean, be expected to lead to an initially compensated warming and salinification at the surface. In addition to providing more salty water to the surface, a warmer surface leads to enhanced heat loss and evaporation and enhanced light-to-dense water mass transformation at the surface in the North Atlantic. Thus, one would expect an intensification of NADW formation and the interhemispheric overturning cell under an increase in κ_n. This is opposite to the changes we see in the HIGH experiment. However, we note that NADW formation in low-resolution ocean models may be sensitive to other parameters, such as the surface salinity restoring rate ($\sim$ 40m/365 days in ACCESS-OM2, on the lower end of many of the models participating in the Ocean Model Intercomparison Program, OMIP-2, Tsujino et al. (2020)). The contribution of Northern Hemisphere versus Southern Hemisphere processes to the control of the interhemispheric overturning cell is still under debate (e.g. Bishop et al., 2016; Delworth & Zeng, 2008; Hogg et al., 2017; Jochum & Eden, 2015). The drivers likely depend on the response time-scale (here we examine quasi-equilibrium simulations).

3.9 The Antarctic bottom water cell

The anomalies in overturning in HIGH and LOW emphasize that changes in the interhemispheric cell are often accompanied by changes in the bottom water cell of the opposite sign. This may arise from a competition between conversion of water upwelled in the Southern Ocean; when more water is converted into lighter mode and interme-

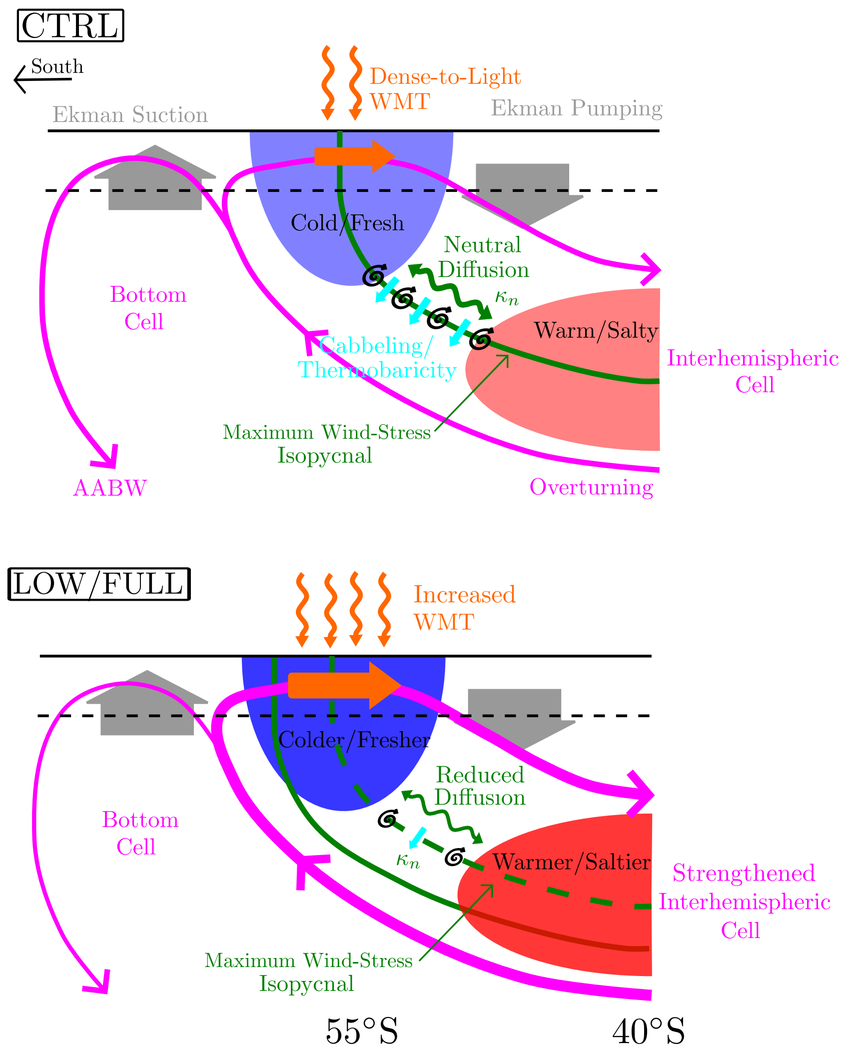

Figure 13. A schematic illustrating how changes in κ_n influence the strength of the interhemispheric overturning cell through a zonal average across the Southern Ocean. In CTRL (top) the maximum overturning occurs along the isopycnal (green line) whose outcrop separates the Ekman suction to the south from Ekman pumping to the north (large gray arrows). Across this isopycnal there is dense-to-light watermass transformation (thick orange arrow) driven by the surface buoyancy flux into the ocean (curly orange arrows). Along this isopycnal, surface waters are cold/fresh (blue region) while deeper waters are warm/salty (red region), with the strength of this gradient influenced by neutral diffusion (green curly arrow). Cabbeling and thermobaricity (cyan lines) drive some light-to-dense transformation along these gradients. The interhemispheric and bottom water overturning cells are illustrated in magenta.
When κ_n is reduced (as in LOW or FULL, bottom) along-isopycnal temperature-salinity contrasts are increased leading to cooling/freshening at the surface and warming/salinification at depth. The surface buoyancy flux into the ocean increases in response to surface cooling, leading to increased dense-to-light watermass transformation (orange arrow). The lighter surface waters are carried into the interior along the downwelling arm of the interhemispheric overturning cell, which combined with reduced cabbeling/thermobaricity leads to a lightening of the upper ocean in the mid-latitudes (illustrated by a southward shift of isopycnals illustrated with green lines). This lightening of the upper mid-latitude oceans results in an increased mid-latitude stratification that strengthens the interhemispheric overturning cell through thermal wind balance (e.g. Wolfe & Cessi, 2010, thick magenta line in bottom panel).

diate waters as part of the interhemispheric cell less is converted into denser waters and enters the bottom water cell, and vice versa. Indeed, when κ_n is increased (HIGH), the surface density is increased around the entire Southern Ocean, resulting in larger areas of deeper mixed-layers and indicating enhanced bottom water formation (Fig. 14b). In LOW the response is largely opposite of that in HIGH (Fig. 14c). However, in FULL the surface density anomalies, while having a similar pattern to those in LOW, are significantly reduced in amplitude (Fig. 14d). Similarly, the shoaling of deep mixed layers is much reduced in FULL. This is linked to the stronger neutral diffusion in FULL compared to LOW across much of the interior Southern Ocean (compare Figs. 14e,f) which supplies heat to the surface. As a consequence, the FULL experiment largely maintains its formation of Antarctic bottom water in contrast to LOW (e.g. compare Figs. 4e and 4k).

4 Summary and Discussion

In this study, we have examined the impact of varying physics-based choices for the spatial structure of the neutral diffusivity κ_n arising from unresolved mesoscale eddy stirring, based on the theory and observational study of Groeskamp et al. (2020), on a coarse-resolution global ocean sea-ice model (ACCESS-OM2). We show that ACCESS-OM2's overturning circulation and tracer structure are sensitive to both the magnitude and the spatial structure of κ_n. Results can be summarized as follows:

1. In general, stronger (weaker) neutral diffusion leads to a weakening (strengthening) in the interhemispheric overturning cell through changes in SST and surface heat, freshwater and buoyancy flux-driven watermass transformation, along with changes in cabbeling and thermobaricity, in the Southern Ocean (as summarized in the schematic in Fig. 13). Changes of ±2Sv (or up to 20%) were found in the interhemispheric cell across our suite of experiments (Figs. 3c, 4). As the surface winds are fixed in these experiments, these changes highlight not only the importance of neutral diffusion, but also of buoyancy forcing for the modeled overturning circulation.
2. Our results suggest that the vertical structure based on surface-mode theory (LaCasce, 2017) in κ_n has only a modest impact on circulation and tracer fields (compare MLT2D and MLT3D in Figs. 4,7). In general, κ_n variations at high-latitudes had stronger impacts than at low-latitudes. Most importantly, the effects of mixing suppression by mean-flows (Ferrari & Nikurashin, 2010) were first-order. Mean-flow suppression reduced κ_n throughout much of the ocean (particularly near the surface, compare Figs. 2b,d) and strongly impacted the circulation and tracer structure (compared to simulations utilizing mixing length theory only).
3. The spatial structure for κ_n based on the "best guess" configuration from Groeskamp et al. (2020) in experiment FULL showed the best overall match to observations taking into account the magnitudes of the 1) interhemispheric cell, 2) bottom water cell and 3) zonal mean tracer biases. In particular, the FULL experiment achieved a stronger interhemispheric cell without reducing the bottom water cell, unlike in the spatially-uniform reduction experiment LOW. The use of the FULL spatial structure for κ_n leads to better agreement between the coarse-resolution ACCESS-OM2 overturning circulation and meridional heat transport with the high-resolution ACCESS-OM2-025 and ACCESS-OM2-01 configurations (Kiss et al., 2020), where the spatial structure of mesoscale eddy-driven stirring is better resolved.

While drawing strong conclusions from a single-model study must be treated with caution given the potential for error compensation, the sensitivity of circulation and hydrography to κ_n motivates further investigation of the use of the Groeskamp et al. (2020) scheme as a parameterization. However, before use for production purposes further work is needed. For example, the model stratification and flow fields should be used for the

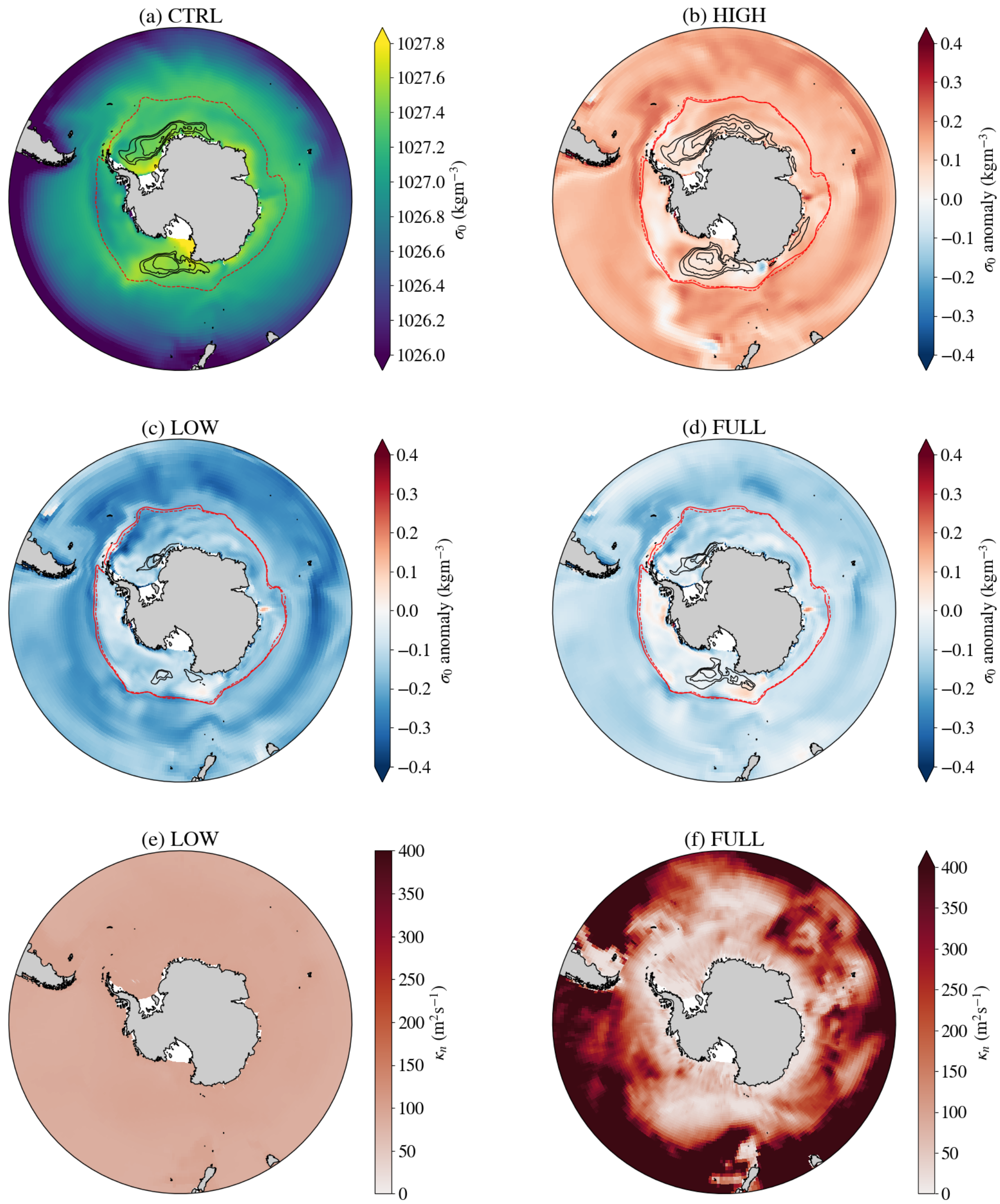

Figure 14. Annual-mean surface density (σ_0, kg m^{-3}) plots south of 40°S for (a) CTRL and anomalies from CTRL for the (b) HIGH, (c) LOW and (d) FULL experiments. The annual-mean mixed layer depth is contoured at 500 m intervals in black. The red contours indicates the monthly-maximum 50% sea-ice extent (CTRL with dashed contours, HIGH, LOW and FULL with solid contours). Surface values of the neutral diffusivity in (e) LOW and (f) FULL.

calculation of modes, the deformation radius and the mean-flow suppression factor. The theory could also be combined with a 2D dynamical model for the EKE field (e.g. Adcroft et al., 2019; Jansen et al., 2015). We also note that while the use of an ocean-only model here helped with the attribution of cause and effect, a similar study performed in a coupled atmosphere-ocean model is needed to evaluate the impact of additional wind, buoyancy and sea-ice feedbacks (e.g. Pradal & Gnanadesikan, 2014) that may complicate the response.

We have focused on the neutral diffusivity κ_n in this article and have not discussed similar changes in κ_{GM}. Preliminary experiments indicate that, while spatially-uniform changes in κ_{GM} equivalent to HIGH and LOW have a larger impact on circulation than κ_n, more subtle changes in its structure (e.g. equivalent to FULL vs. CTRL with $\kappa_{GM} = \kappa_n$) induce circulation and zonal mean tracer anomalies no larger than those associated with κ_n only. While further work is required, and more sophisticated theories for κ_{GM} and the inclusion of eddy effects on momentum and energy already exist, these results suggest that κ_n deserves more attention in coarse-resolution model sensitivity studies.

Acknowledgments
We thank J. Zika for helpful comments. We thank the Consortium for Ocean and Sea-Ice Modelling in Australia (COSIMA) community for their valuable contributions to ACCESS-OM2 development. Modeling and analysis were undertaken using facilities at the National Computational Infrastructure (NCI), which is supported by the Australian Government. R Holmes and T. McDougall gratefully acknowledge Australian Research Council (ARC) support through grant FL150100090. R Holmes acknowledges support from ARC award DE21010004. Upon acceptance, the data required to reproduce the results in this article will be published online at Zenodo and the digital object identifier (doi) will be quoted here.

References

Abernathey, R., Ferreira, D., & Klocker, A. (2013). Diagnostics of isopycnal mixing in a circumpolar channel. *Ocean Model.*, *72*, 1 - 16. doi: 10.1016/j.ocemod.2013.07.004
Abernathey, R., Marshall, J., Mazloff, M., & Shuckburgh, E. (2010). Enhancement of mesoscale eddy stirring at steering levels in the southern ocean. *J. Phys. Oceanogr.*, *40*, 170-184.
Adcroft, A., Anderson, W., Balaji, V., Blanton, C., Bushuk, M., Dufour, C. O., . . . Zhang, R. (2019). The GFDL Global Ocean and Sea Ice Model OM4.0: Model description and simulation features. *J. Adv. Model. Earth Syst.*, *11*, 3167-3211. doi: 10.1029/2019MS001726
Bachman, S. D., Fox-Kemper, B., & Bryan, F. O. (2020). A diagnosis of anisotropic eddy diffusion from a high-resolution global ocean model. *Journal of Advances in Modeling Earth Systems*, *12*(2), e2019MS001904. doi: 10.1029/2019MS001904
Beckers, J. M., Burchard, H., Campin, J. M., Deleersnijder, E., & Mathieu, P. P. (1998). Another reason why simple discretizations of rotated diffusion operators cause problems in ocean models: Comments on "isoneutral diffusion in a z-coordinate ocean model". *J. Phys. Oceanogr.*, *28*(7), 1552 - 1559. doi: 10.1175/1520-0485(1998)028⟨1552:ARWSDO⟩2.0.CO;2
Beckers, J.-M., Burchard, H., Deleersnijder, E., & Mathieu, P. P. (2000). Numerical discretization of rotated diffusion operators in ocean models. *Mon. Wea. Rev.*, *128*(8), 2711 - 2733. doi: 10.1175/1520-0493(2000)128⟨2711:NDORDO⟩2.0.CO;2
Bishop, S. P., Gent, P. R., Bryan, F. O., Thompson, A. F., Long, M. C., & Abernathey, R. (2016). Southern ocean overturning compensation in an eddy-

resolving climate simulation. *J. Phys. Oceanogr.*, *46*(5), 1575-1592. doi: 10.1175/JPO-D-15-0177.1

Busecke, J. J., & Abernathey, R. P. (2019). Ocean mesoscale mixing linked to climate variability. *Science advances*, *5*(1), eaav5014. doi: 10.1126/sciadv.aav5014

Cessi, P. (2008). An energy-constrained parameterization of eddy buoyancy flux. *J. Phys. Oceanogr.*, *38*(8), 1807 - 1819. doi: 10.1175/2007JPO3812.1

Danabasoglu, G., & Marshall, J. (2007). Effects of vertical variations of thickness diffusivity in an ocean general circulation model. *Ocean Model.*, *18*(2), 122 - 141. doi: 10.1016/j.ocemod.2007.03.006

Danabasoglu, G., & McWilliams, J. C. (1995). Sensitivity of the global ocean circulation to parameterizations of mesoscale tracer transports. *J. Climate*, *8*(12), 2967 - 2987. doi: 10.1175/1520-0442(1995)008⟨2967:SOTGOC⟩2.0.CO;2

de Lavergne, C., Groeskamp, S., Zika, J., & Johnson, H. L. (2022). Chapter 3 - the role of mixing in the large-scale ocean circulation. In M. Meredith & A. Naveira Garabato (Eds.), *Ocean mixing* (p. 35-63). Elsevier. doi: 10.1016/B978-0-12-821512-8.00010-4

Delworth, T. L., & Zeng, F. (2008). Simulated impact of altered Southern Hemisphere winds on the Atlantic Meridional Overturning Circulation. *Geophys. Res. Lett.*, *35*(20). doi: 10.1029/2008GL035166

Döös, K., & Webb, D. J. (1994). The Deacon Cell and the Other Meridional Cells of the Southern Ocean. *J. Phys. Oceanogr.*, *24*(2), 429-442. doi: 10.1175/1520-0485(1994)024⟨0429:TDCATO⟩2.0.CO;2

Eden, C., & Greatbatch, R. J. (2008). Towards a mesoscale eddy closure. *Ocean Model.*, *20*(3), 223-239. doi: 10.1016/j.ocemod.2007.09.002

Eden, C., Jochum, M., & Danabasoglu, G. (2009). Effects of different closures for thickness diffusivity. *Ocean Model.*, *26*(1), 47-59. doi: 10.1016/j.ocemod.2008.08.004

England, M. H., & Rahmstorf, S. (1999). Sensitivity of ventilation rates and radiocarbon uptake to subgrid-scale mixing in ocean models. *J. Phys. Oceanogr.*, *29*(11), 2802 - 2828. doi: 10.1175/1520-0485(1999)029⟨2802:SOVRAR⟩2.0.CO;2

Ferrari, R., McWilliams, J. C., Canuto, V. M., & Dubovikov, M. (2008). Parameterization of eddy fluxes near oceanic boundaries. *J. Climate*, *21*(12), 2770-2789. doi: 10.1175/2007JCLI1510.1

Ferrari, R., & Nikurashin, M. (2010, 07). Suppression of Eddy Diffusivity across Jets in the Southern Ocean. *J. Phys. Oceanogr.*, *40*(7), 1501-1519. doi: 10.1175/2010JPO4278.1

Ferreira, D., Marshall, J., & Heimbach, P. (2005). Estimating eddy stresses by fitting dynamics to observations using a residual-mean ocean circulation model and its adjoint. *J. Phys. Oceanogr.*, *35*(10), 1891 - 1910. doi: 10.1175/JPO2785.1

Gent, P. R. (2011). The Gent-McWilliams parameterization: 20/20 hindsight. *Ocean Model.*, *39*(1?2), 2 - 9. (Modelling and Understanding the Ocean Mesoscale and Submesoscale) doi: 10.1016/j.ocemod.2010.08.002

Gent, P. R., & McWilliams, J. C. (1990). Isopycnal mixing in ocean circulation models. *J. Phys. Oceanogr.*, *20*(1), 150–155. doi: 10.1175/1520-0485(1990)020⟨0150:IMIOCM⟩2.0.CO;2

Gnanadesikan, A., Dixon, K. W., Griffies, S. M., Balaji, V., Barreiro, M., Beesley, J. A., ... Dunne, J. P. (2006). GFDL's CM2 Global Coupled Climate Models. Part II: The Baseline Ocean Simulation. *J. Climate*, *19*(5), 675 - 697. doi: 10.1175/JCLI3630.1

Gnanadesikan, A., Pradal, M.-A., & Abernathey, R. (2015). Isopycnal mixing by mesoscale eddies significantly impacts oceanic anthropogenic carbon uptake. *Geophys. Res. Lett.*, *42*(11), 4249-4255. doi: 10.1002/2015GL064100

Gnanadesikan, A., Russell, A., Pradal, M.-A., & Abernathey, R. (2017). Impact of lateral mixing in the ocean on El Nino in a suite of fully coupled climate models. *J. Adv. Model. Earth Syst.*, *9*. doi: 10.1002/2017MS000917

Gough, W., & Lin, C. (1995). Isopycnal mixing and the Veronis effect in an ocean general circulation model. *Journal of Marine Research*, *53*, 189-199. doi: 10.1357/0022240953213223

Griffies, S. M. (1998). The Gent-McWilliams skew flux. *J. Phys. Oceanogr.*, *28*(5), 831-841. doi: 10.1175/1520-0485(1998)028⟨0831:TGMSF⟩2.0.CO;2

Griffies, S. M. (2012). Elements of the modular ocean model (MOM). *GFDL Ocean Group Tech. Rep*, *7*, 620.

Griffies, S. M., Gnanadesikan, A., Dixon, K. W., Dunne, J. P., Gerdes, R., Harrison, M. J., … Zhang, R. (2005, Sep). Formulation of an ocean model for global climate simulations. *Ocean Science*, *1*(1), 45-79.

Griffies, S. M., Gnanadesikan, A., Pacanowski, R. C., Larichev, V., Dukowicz, J. K., & Smith, R. D. (1998). Isoneutral diffusion in a z-coordinate ocean model. *J. Phys. Oceanogr.*, *28*, 805–830. doi: 10.1175/1520-0485(1998)028⟨0805:IDIAZC⟩2.0.CO;2

Griffies, S. M., Harrison, M. J., Pacanowski, R. C., & Rosati, A. (2004). A technical guide to MOM4. *GFDL Ocean Group Tech. Rep*, *5*, 371.

Griffies, S. M., Winton, M., Anderson, W. G., Benson, R., Delworth, T. L., Dufour, C. O., … Zhang, R. (2015). Impacts on ocean heat from transient mesoscale eddies in a hierarchy of climate models. *J. Climate*, *28*(3), 952-977. doi: 10.1175/JCLI-D-14-00353.1

Groeskamp, S., Abernathey, R. P., & Klocker, A. (2016). Water mass transformation by cabbeling and thermobaricity. *Geophys. Res. Lett.*, *43*. (2016GL070860) doi: 10.1002/2016GL070860

Groeskamp, S., Barker, P. M., McDougall, T. J., Abernathey, R. P., & Griffies, S. M. (2019). VENM: An algorithm to accurately calculate neutral slopes and gradients. *J. Adv. Model. Earth Syst.*, *11*(7), 1917-1939. doi: 10.1029/2019MS001613

Groeskamp, S., LaCasce, J. H., McDougall, T. J., & Rogè, M. (2020). Full-depth global estimates of ocean mesoscale eddy mixing from observations and theory. *Geophys. Res. Lett.*, *47*(18), e2020GL089425. doi: 10.1029/2020GL089425

Guilyardi, É., Madec, G., & Terray, L. (2001). The role of lateral ocean physics in the upper ocean thermal balance of a coupled ocean-atmosphere GCM. *Climate Dynamics*, *17*(8), 589–599. doi: 10.1007/PL00007930

Hallberg, R. (2013). Using a resolution function to regulate parameterizations of oceanic mesoscale eddy effects. *Ocean Model.*, *72*, 92 - 103. doi: 10.1016/j.ocemod.2013.08.007

Hieronymus, M., & Nycander, J. (2013). The budgets of heat and salinity in NEMO. *Ocean Model.*, *67*, 28 - 38. doi: 10.1016/j.ocemod.2013.03.006

Hogg, A. M., Spence, P., Saenko, O. A., & Downes, S. M. (2017). The Energetics of Southern Ocean Upwelling. *J. Phys. Oceanogr.*, *47*(1), 135-153. doi: 10.1175/JPO-D-16-0176.1

Holmes, R. M., Zika, J. D., Griffies, S. M., Hogg, A. M., Kiss, A. E., & England, M. H. (2021). The geography of numerical mixing in a suite of global ocean models. *J. Adv. Model. Earth Syst.*, *13*(7), e2020MS002333. doi: 10.1029/2020MS002333

Hunke, E. C., Lipscomb, W. H., Turner, A. K., Jeffery, N., & Elliott, S. (2015). CICE: The Los Alamos Sea Ice Model Documentation and Software User's Manual Version 5.1. *Tech. Rep. LA-CC-06-012, Los Alamos National Laboratory*.

Jackett, D. R., McDougall, T. J., Feistel, R., Wright, D. G., & Griffies, S. M. (2006). Algorithms for density, potential temperature, conservative temperature, and the freezing temperature of seawater. *J. Atmos. Ocean Technol.*, *23*(12), 1709 -

1728. doi: 10.1175/JTECH1946.1

Jansen, M. F., Adcroft, A., Khani, S., & Kong, H. (2019). Toward an energetically consistent, resolution aware parameterization of ocean mesoscale eddies. *J. Adv. Model. Earth Syst.*, *11*(8), 2844-2860. doi: 10.1029/2019MS001750

Jansen, M. F., Adcroft, A. J., Hallberg, R., & Held, I. M. (2015). Parameterization of eddy fluxes based on a mesoscale energy budget. *Ocean Model.*, *92*, 28 - 41. doi: 10.1016/j.ocemod.2015.05.007

Jansen, M. F., & Held, I. M. (2014). Parameterizing subgrid-scale eddy effects using energetically consistent backscatter. *Ocean Model.*, *80*, 36-48. doi: 10.1016/j.ocemod.2014.06.002

Jochum, M., & Eden, C. (2015, sep). The connection between Southern Ocean winds, the Atlantic meridional overturning circulation, and Indo-Pacific upwelling. *J. Climate*, *28*(23), 9250–9257. doi: 10.1175/JCLI-D-15-0263.1

Johns, T. C., Durman, C. F., Banks, H. T., Roberts, M. J., McLaren, A. J., Ridley, J. K., ... Searl, Y. (2006). The New Hadley Centre Climate Model (HadGEM1): Evaluation of Coupled Simulations. *J. Climate*, *19*(7), 1327 - 1353. doi: 10.1175/JCLI3712.1

Jones, C. S., & Abernathey, R. P. (2019). Isopycnal mixing controls deep ocean ventilation. *Geophys. Res. Lett.*, *46*(22), 13144-13151. doi: 10.1029/2019GL085208

Jones, C. S., & Abernathey, R. P. (2021). Modeling water-mass distributions in the modern and lgm ocean: circulation change, isopycnal and diapycnal mixing. *J. Phys. Oceanogr.*. doi: 10.1175/JPO-D-20-0204.1

Jungclaus, J. H., Lorenz, S. J., Timmreck, C., Reick, C. H., Brovkin, V., Six, K., ... Marotzke, J. (2010). Climate and carbon-cycle variability over the last millennium. *Climate of the Past*, *6*(5), 723–737. doi: 10.5194/cp-6-723-2010

Juricke, S., Danilov, S., Koldunov, N., Oliver, M., Sein, D. V., Sidorenko, D., & Wang, Q. (2020). A kinematic kinetic energy backscatter parametrization: From implementation to global ocean simulations. *J. Adv. Model. Earth Syst.*, *12*(12), e2020MS002175. doi: 10.1029/2020MS002175

Kiss, A. E., Hogg, A. M., Hannah, N., Boeira Dias, F., Brassington, G. B., Chamberlain, M. A., ... Zhang, X. (2020). ACCESS-OM2 v1.0: A global ocean–sea ice model at three resolutions. *Geosci. Model Dev.*, *13*(2), 401–442. doi: 10.5194/gmd-13-401-2020

Klocker, A., & Abernathey, R. (2013). Global patterns of mesoscale eddy properties and diffusivities. *J. Phys. Oceanogr.*, *44*(3), 1030–1046.

Klocker, A., & McDougall, T. J. (2010). Influence of the nonlinear equation of state on global estimates of dianeutral advection and diffusion. *J. Phys. Oceanogr.*, *40*(8), 1690–1709. doi: 10.1175/2010JPO4303.1

LaCasce, J. H. (2017). The prevalence of oceanic surface modes. *Geophys. Res. Lett.*, *44*, 11097-11105. (2017GL075430) doi: 10.1002/2017GL075430

LaCasce, J. H., & Groeskamp, S. (2020, 08). Baroclinic modes over rough bathymetry and the surface deformation radius. *J. Phys. Oceanogr.*, 1-40. doi: 10.1175/JPO-D-20-0055.1

Large, W., & Yeager, S. (2004). *Diurnal to decadal global forcing for ocean and sea-ice models: the data sets and flux climatologies.* National Center for Atmospheric Research.

Lemarié, F., Debreu, L., Shchepetkin, A., & McWilliams, J. (2012). On the stability and accuracy of the harmonic and biharmonic isoneutral mixing operators in ocean models. *Ocean Model.*, *52-53*, 9-35. doi: 10.1016/j.ocemod.2012.04.007

Locarnini, R. A., Mishonov, A. V., Antonov, J. I., Boyer, T. P., Garcia, H. E., Baranova, O. K., ... Seidov, D. (2013). World Ocean Atlas 2013, Volume 1: Temperature. *NOAA Atlas NESDIS*, *73*, 40. (S. Levitus, Ed., A. Mishonov Technical Ed.)

Marshall, D. P., & Adcroft, A. J. (2010). Parameterization of ocean eddies: Potential vorticity mixing, energetics and arnold's first stability theorem. *Ocean Model.*, *32*(3), 188-204. doi: 10.1016/j.ocemod.2010.02.001

McCarthy, G. D., Smeed, D. A., Johns, W. E., Frajka-Williams, E., Moat, B. I., Rayner, D., ... Bryden, H. L. (2015). Measuring the Atlantic Meridional Overturning Circulation at 26N. *Prog. Oceanogr.*, *130*, 91–111. doi: 10.1016/j.pocean.2014.10.006

McDougall, T. (1987). Thermobaricity, cabbeling, and water-mass conversion. *J. Geophys. Res. Oceans*, *92*(C5), 5448-5464. doi: 10.1029/JC092iC05p05448

McDougall, T. J. (2003). Potential enthalpy: A conservative oceanic variable for evaluating heat content and heat fluxes. *J. Phys. Oceanogr.*, *33*(5), 945-963. doi: 10.1175/1520-0485(2003)033⟨0945:PEACOV⟩2.0.CO;2

McDougall, T. J., & Barker, P. M. (2011). Getting started TEOS-10 and the Gibbs Seawater (GSW) oceanographic toolbox. *SCOR/IAPSO WG*, *127*, 1–28.

McDougall, T. J., & Church, J. A. (1986). Pitfalls with the numerical representation of isopycnal diapycnal mixing. *J. Phys. Oceanogr.*, *16*(1), 196 - 199. doi: 10.1175/1520-0485(1986)016⟨0196:PWTNRO⟩2.0.CO;2

McDougall, T. J., Groeskamp, S., & Griffies, S. M. (2014). On geometrical aspects of interior ocean mixing. *J. Phys. Oceanogr.*, *44*(8), 2164-2175. doi: 10.1175/JPO-D-13-0270.1

Meijers, A. J. S. (2014). The Southern Ocean in the Coupled Model Intercomparison Project phase 5. *Philosophical Transactions of the Royal Society A: Mathematical, Physical and Engineering Sciences*, *372*(2019), 20130296. doi: 10.1098/rsta.2013.0296

Morrison, A. K., Saenko, O. A., Hogg, A. M., & Spence, P. (2013). The role of vertical eddy flux in southern ocean heat uptake. *Geophys. Res. Lett.*, *40*(20), 5445-5450. doi: 10.1002/2013GL057706

Nycander, J., Hieronymus, M., & Roquet, F. (2015). The nonlinear equation of state of sea water and the global water mass distribution. *Geophysical Research Letters*, *42*(18), 7714-7721. doi: 10.1002/2015GL065525

Pearson, B., Fox-Kemper, B., Bachman, S., & Bryan, F. (2017). Evaluation of scale-aware subgrid mesoscale eddy models in a global eddy-rich model. *Ocean Model.*, *115*, 42-58. doi: 10.1016/j.ocemod.2017.05.007

Pradal, M.-A., & Gnanadesikan, A. (2014). How does the redi parameter for mesoscale mixing impact global climate in an earth system model? *J. Adv. Model. Earth Syst.*, *6*(3), 586-601. doi: 10.1002/2013MS000273

Prandtl, L. (1925). Report on investigation of developed turbulence. *NACA Report TM-1231*.

Redi, M. H. (1982). Oceanic isopycnal mixing by coordinate rotation. *J. Phys. Oceanogr.*, *12*(10), 1154-1158. doi: 10.1175/1520-0485(1982)012⟨1154:OIMBCR⟩2.0.CO;2

Shao, A. E., Adcroft, A., Hallberg, R., & Griffies, S. M. (2020). A general-coordinate, nonlocal neutral diffusion operator. *J. Adv. Model. Earth Syst.*, *12*(12), e2019MS001992. doi: 10.1029/2019MS001992

Sijp, W. P., Bates, M., & England, M. H. (2006). Can isopycnal mixing control the stability of the thermohaline circulation in ocean climate models? *J. Climate*, *19*(21), 5637 - 5651. doi: 10.1175/JCLI3890.1

Sijp, W. P., & England, M. H. (2009). The control of polar haloclines by along-isopycnal diffusion in climate models. *J. Climate*, *22*(3), 486 - 498. doi: 10.1175/2008JCLI2513.1

Smith, K. S., & Marshall, J. (2009). Evidence for Enhanced Eddy Mixing at Middepth in the Southern Ocean. *J. Phys. Oceanogr.*, *39*(1), 50-69. doi: 10.1175/2008JPO3880.1

Smith, K. S., & Vallis, G. K. (2002). The scales and equilibration of midocean eddies: Forced?dissipative flow. *J. Phys. Oceanogr.*, *32*(6), 1699 - 1720. doi: 10.1175/1520-0485(2002)032⟨1699:TSAEOM⟩2.0.CO;2

Solomon, H. (1971, 07). On the Representation of Isentropic Mixing in Ocean Circulation Models. *J. Phys. Oceanogr.*, *1*(3), 233-234. doi: 10.1175/1520-0485(1971)001⟨0233:OTROIM⟩2.0.CO;2

Stanley, Z., Bachman, S., & Grooms, I. (2020). Vertical structure of ocean mesoscale eddies with implications for parameterizations of tracer transport. *J. Adv. Model. Earth Syst.*, e2020MS002151.

Stewart, K., & Hogg, A. (2019). Southern ocean heat and momentum uptake are sensitive to the vertical resolution at the ocean surface. *Ocean Model.*, *143*, 101456. doi: 10.1016/j.ocemod.2019.101456

Stewart, K., Hogg, A., England, M., Waugh, D., & Kiss, A. (2021). The Ekman streamfunction and the Eulerian and residual overturning circulations of the Southern Ocean. *Geophys. Res. Lett.*, *48*, e2021GL093438. (e2021GL093438 2021GL093438) doi: 10.1029/2021GL093438

Stewart, K., Hogg, A., Griffies, S., Heerdegen, A., Ward, M., Spence, P., & England, M. (2017). Vertical resolution of baroclinic modes in global ocean models. *Ocean Model.*, *113*, 50 - 65. doi: 10.1016/j.ocemod.2017.03.012

Stewart, K., Kim, W., Urakawa, S., Hogg, A., Yeager, S., Tsujino, H., ... Danabasoglu, G. (2019). JRA55-do-based repeat year forcing datasets for driving ocean-sea-ice models. *Ocean Model.*, 101557. doi: 10.1016/j.ocemod.2019.101557

Treguier, A. M., Held, I. M., & Larichev, V. D. (1997). Parameterization of quasigeostrophic eddies in primitive equation ocean models. *J. Phys. Oceanogr.*, *27*(4), 567 - 580. doi: 10.1175/1520-0485(1997)027⟨0567:POQEIP⟩2.0.CO;2

Tsujino, H., Urakawa, L. S., Griffies, S. M., Danabasoglu, G., Adcroft, A. J., Amaral, A. E., ... Yu, Z. (2020). Evaluation of global ocean sea-ice model simulations based on the experimental protocols of the Ocean Model Intercomparison Project phase 2 (OMIP-2). *Geoscientific Model Development Discussions*, *2020*, 1–86. doi: 10.5194/gmd-2019-363

Tsujino, H., Urakawa, S., Nakano, H., Small, R. J., Kim, W. M., Yeager, S. G., ... others (2018). JRA-55 based surface dataset for driving ocean–sea-ice models (JRA55-do). *Ocean Model.*, *130*, 79–139. doi: 10.1016/j.ocemod.2018.07.002

Urakawa, L. S., Tsujino, H., Nakano, H., Sakamoto, K., Yamanaka, G., & Toyoda, T. (2020). The sensitivity of a depth-coordinate model to diapycnal mixing induced by practical implementations of the isopycnal tracer diffusion scheme. *Ocean Model.*, 101693. doi: 10.1016/j.ocemod.2020.101693

Veronis, G. (1975). The role of models in tracer studies. numerical models of the ocean circulation. *Natl. Acad. Sci.*, 133?146.

Visbeck, M., Marshall, J., Haine, T., & Spall, M. (1997). Specification of eddy transfer coefficients in coarse-resolution ocean circulation models. *J. Phys. Oceanogr.*, *27*(3), 381 - 402. doi: 10.1175/1520-0485(1997)027⟨0381:SOETCI⟩2.0.CO;2

Voldoire, A., Sanchez-Gomez, E., y Mélia, D. S., Decharme, B., Cassou, C., Sénési, S., ... others (2013). The CNRM-CM5.1 global climate model: description and basic evaluation. *Climate dynamics*, *40*(9), 2091–2121. doi: 10.1007/s00382-011-1259-y

Vollmer, L., & Eden, C. (2013). A global map of meso-scale eddy diffusivities based on linear stability analysis. *Ocean Model.*, *72*, 198 - 209. doi: 10.1016/j.ocemod.2013.09.006

Williams, P. D., Guilyardi, E., Sutton, R., Gregory, J., & Madec, G. (2007). A new feedback on climate change from the hydrological cycle. *Geophys. Res. Lett.*, *34*(8). doi: 10.1029/2007GL029275

Wolfe, C. L., & Cessi, P. (2010). What sets the strength of the middepth stratification and overturning circulation in eddying ocean models? *J. Phys. Oceanogr.*, *40*(7), 1520 - 1538. doi: 10.1175/2010JPO4393.1

Wolfe, C. L., Cessi, P., McClean, J. L., & Maltrud, M. E. (2008). Vertical heat transport in eddying ocean models. *Geophys. Res. Lett.*, *35*(23). (L23605) doi: 10.1029/2008GL036138

Zweng, M., Reagan, J., Antonov, J., Locarnini, R., Mishonov, A., Boyer, T., … Biddle, M. (2013). World Ocean Atlas 2013, Volume 2: Salinity. *NOAA Atlas NESDIS*, *74*, 39. (S. Levitus, Ed., A. Mishonov Technical Ed.)

Figure 1.

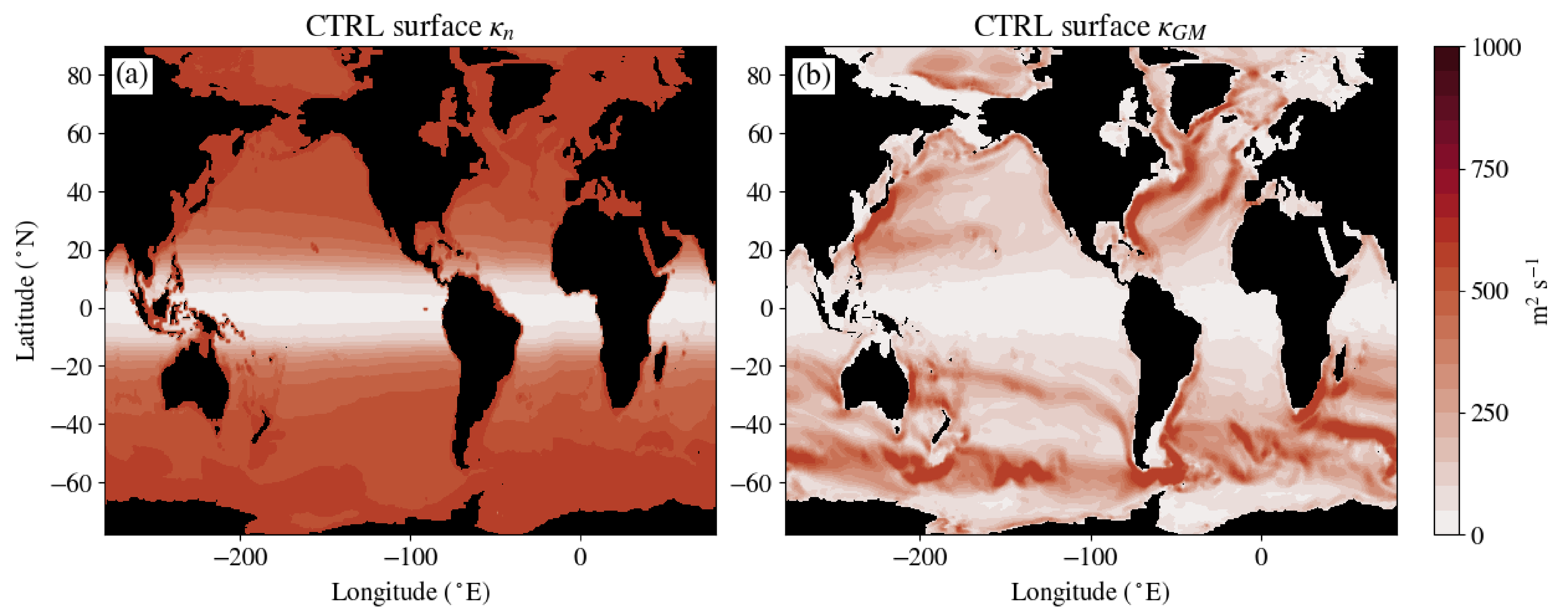

CTRL surface κ_n
CTRL surface κ_{GM}
(a)
(b)
Latitude (°N)
Longitude (°E)
80
60
40
20
0
−20
−40
−60
−200
−100
0
1000
750
500
250
0
$m^2\ s^{-1}$

Figure 2.

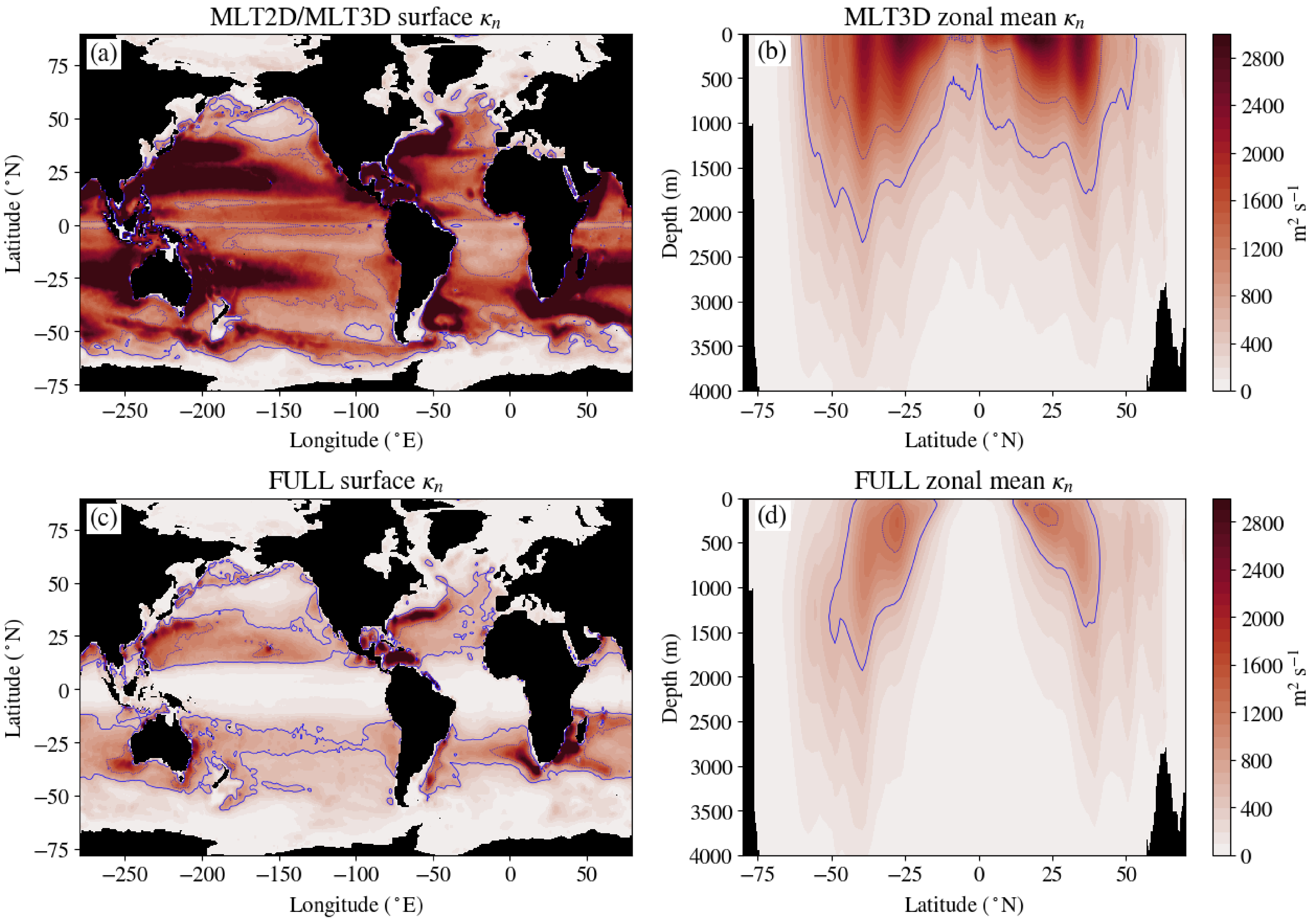

MLT2D/MLT3D surface κ_n
(a)
MLT3D zonal mean κ_n
(b)
FULL surface κ_n
(c)
FULL zonal mean κ_n
(d)
Latitude (°N)
Longitude (°E)
Depth (m)
$m^2\ s^{-1}$

Figure 3.

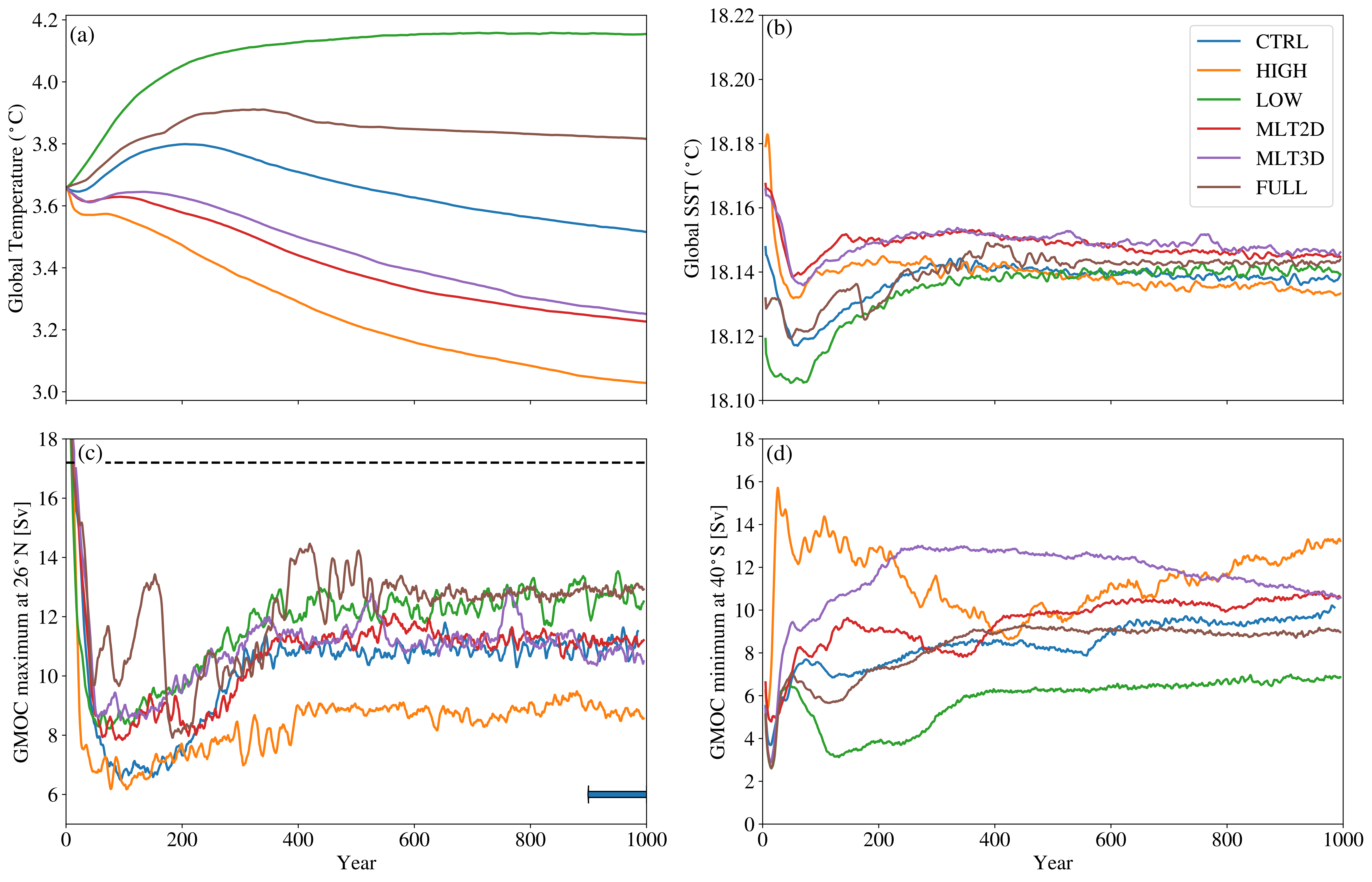

(a)
Global Temperature (°C)
4.2
4.0
3.8
3.6
3.4
3.2
3.0
(b)
Global SST (°C)
18.22
18.20
18.18
18.16
18.14
18.12
18.10
CTRL
HIGH
LOW
MLT2D
MLT3D
FULL
(c)
GMOC maximum at 26°N [Sv]
18
16
14
12
10
8
6
(d)
GMOC minimum at 40°S [Sv]
18
16
14
12
10
8
6
4
2
0
0
200
400
600
800
1000
Year
0
200
400
600
800
1000
Year

Figure 4.

CTRL
(a)
Interhemispheric Cell
Bottom Water Cell
HIGH
(b)
HIGH - CTRL
(c)
LOW
(d)
LOW - CTRL
(e)
MLT2D
(f)
MLT2D - CTRL
(g)
MLT3D
(h)
MLT3D - CTRL
(i)
FULL
(j)
FULL - CTRL
(k)
Potential Density (kg m^{-3})
Latitude (°N)
Sv

Figure 5.

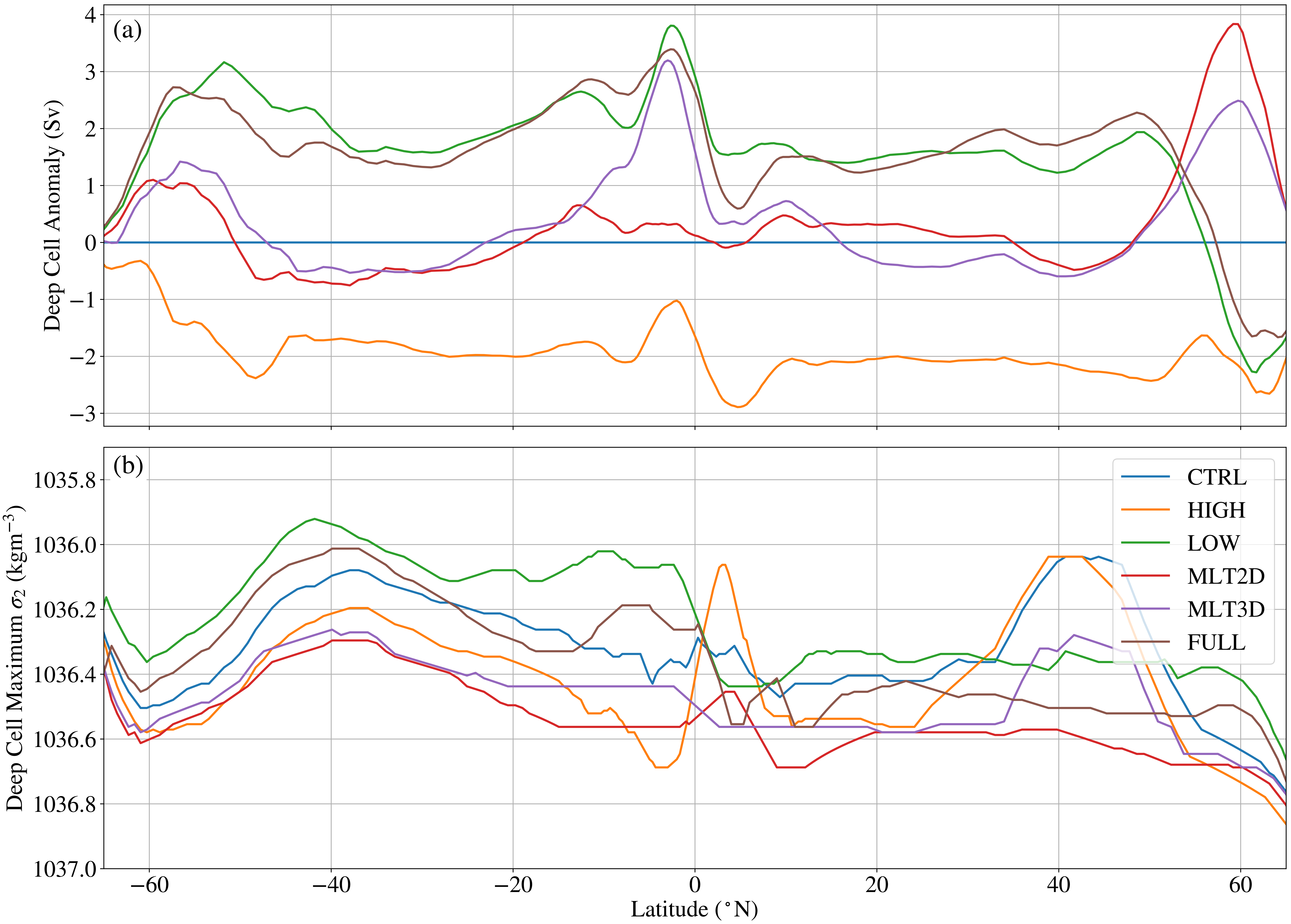
(a)
Deep Cell Anomaly (Sv)
4
3
2
1
0
−1
−2
−3
(b)
Deep Cell Maximum σ_2 (kgm^{-3})
1035.8
1036.0
1036.2
1036.4
1036.6
1036.8
1037.0
−60
−40
−20
0
20
40
60
Latitude (°N)
CTRL
HIGH
LOW
MLT2D
MLT3D
FULL

Figure 6.

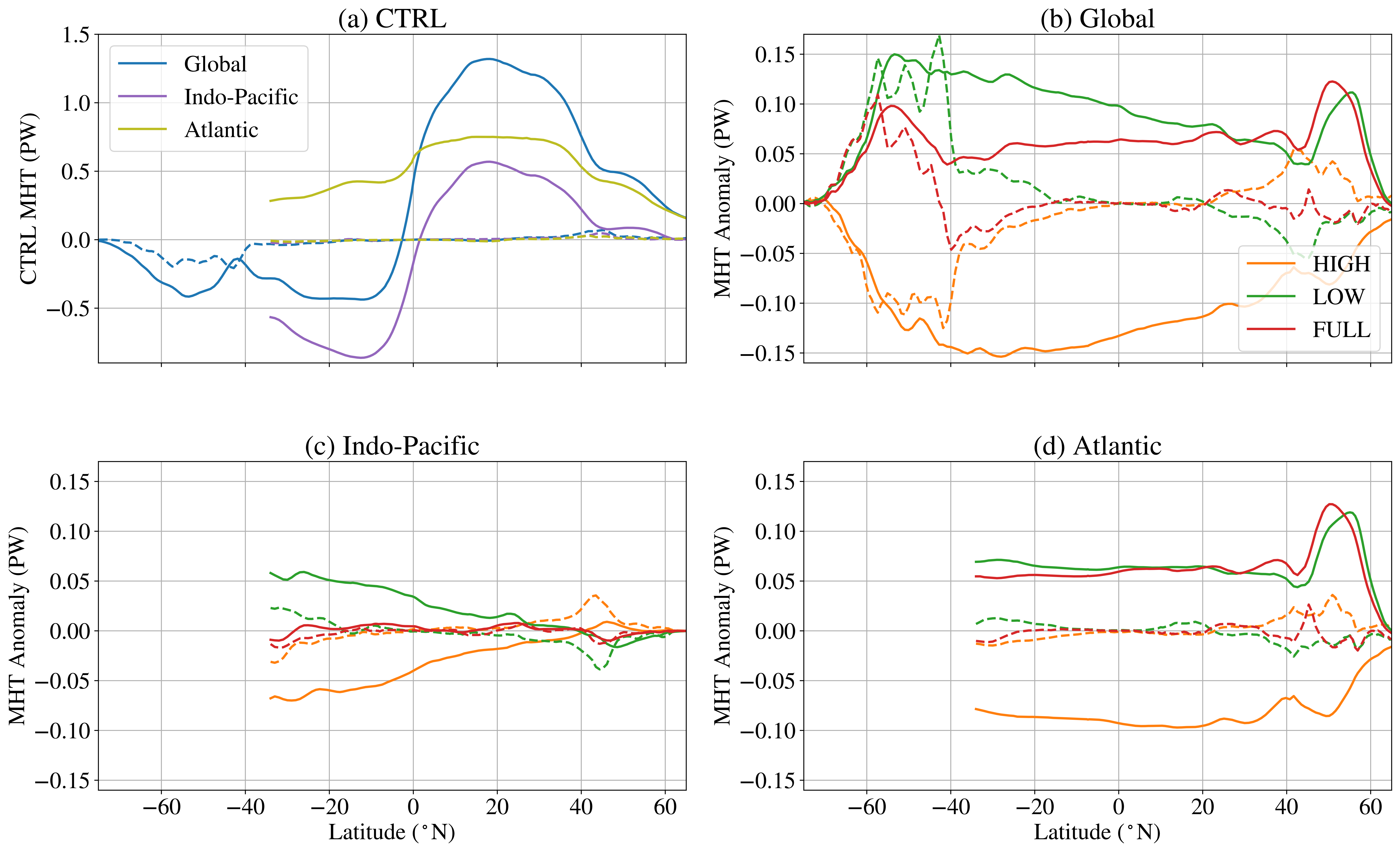
(a) CTRL
(b) Global
(c) Indo-Pacific
(d) Atlantic
Global
Indo-Pacific
Atlantic
HIGH
LOW
FULL
CTRL MHT (PW)
MHT Anomaly (PW)
Latitude (°N)

Figure 7.

CTRL κ_n
CTRL Temperature
CTRL Salinity
CTRL Age
CTRL Temperature WOA13 bias
CTRL Salinity WOA13 bias
HIGH κ_n
HIGH - CTRL Temperature
HIGH - CTRL Salinity
HIGH - CTRL Age
LOW κ_n
LOW - CTRL Temperature
LOW - CTRL Salinity
LOW - CTRL Age
MLT3D κ_n
MLT3D - CTRL Temperature
MLT3D - CTRL Salinity
MLT3D - CTRL Age
FULL κ_n
FULL - CTRL Temperature
FULL - CTRL Salinity
FULL - CTRL Age
Depth (m)
Latitude (°N)
m^2s^{-1}
°C
psu
year

Figure 8.

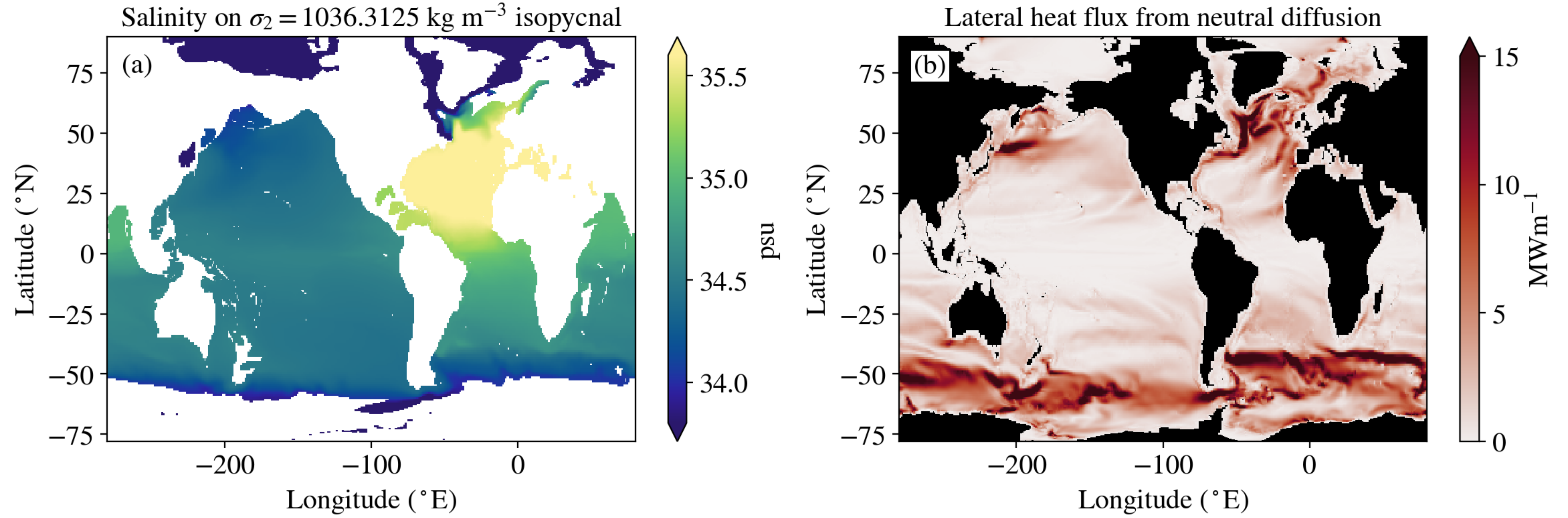

Salinity on $\sigma_2 = 1036.3125$ kg m^{-3} isopycnal
(a)
75
50
25
0
−25
−50
−75
Latitude (°N)
−200
−100
0
Longitude (°E)
35.5
35.0
34.5
34.0
psu
Lateral heat flux from neutral diffusion
(b)
15
10
5
0
MWm^{-1}

Figure 9.

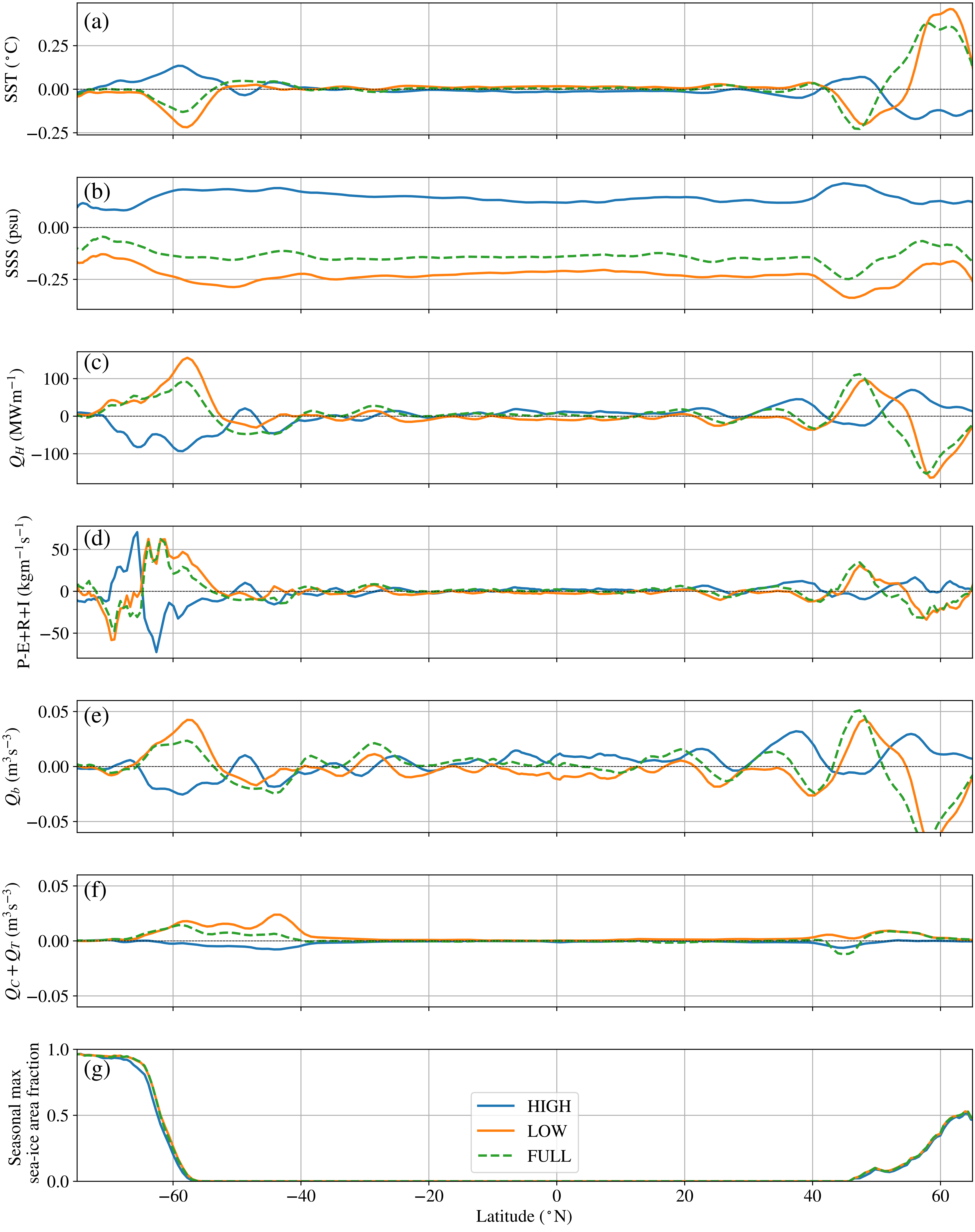

(a)
SST (°C)
(b)
SSS (psu)
(c)
Q_H (MWm^{-1})
(d)
P-E+R+I (kgm^{-1}s^{-1})
(e)
Q_b (m^{3}s^{-3})
(f)
Q_C+Q_T (m^{3}s^{-3})
(g)
Seasonal max sea-ice area fraction
HIGH
LOW
FULL
Latitude (°N)

Figure 10.

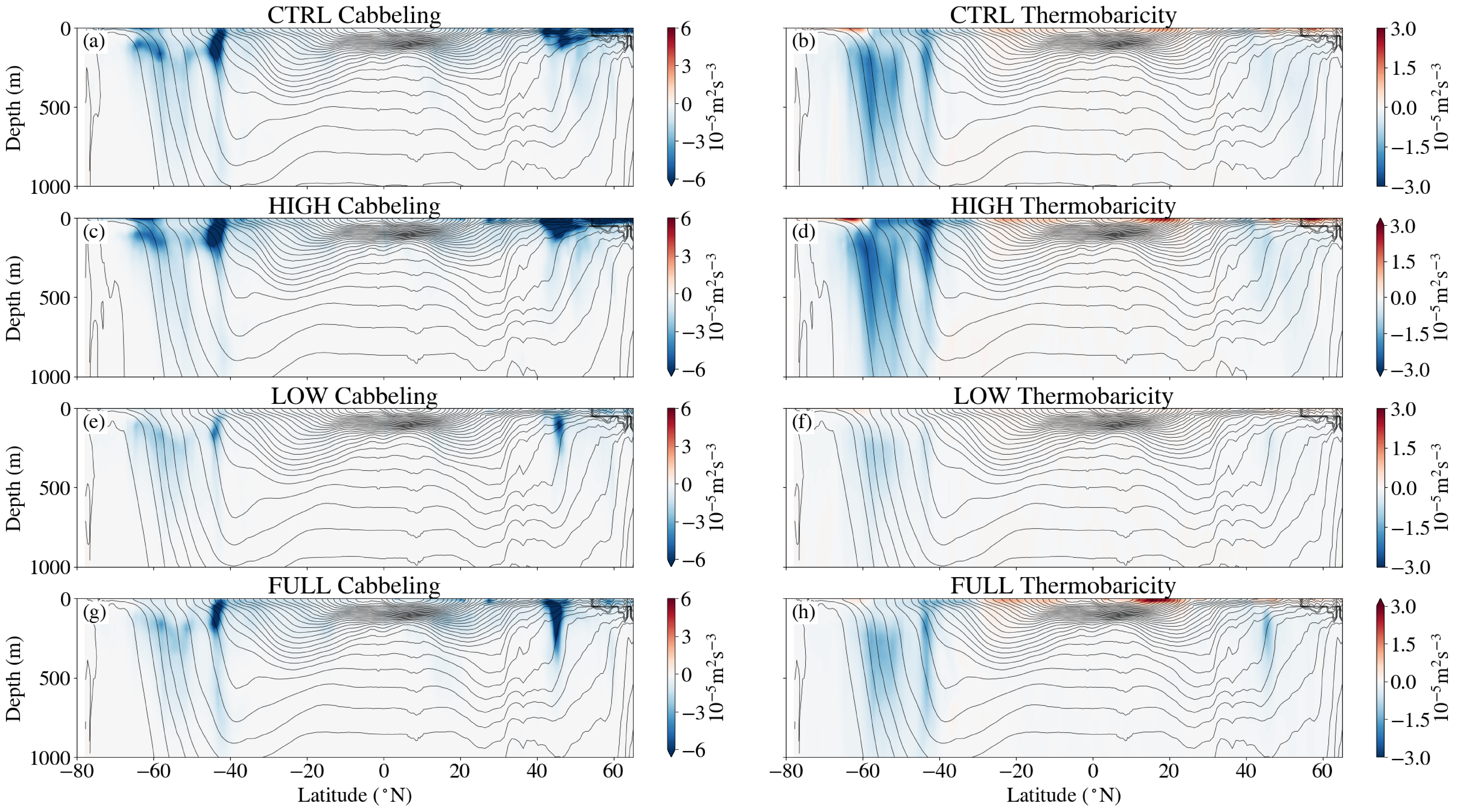

CTRL Cabbeling
CTRL Thermobaricity
HIGH Cabbeling
HIGH Thermobaricity
LOW Cabbeling
LOW Thermobaricity
FULL Cabbeling
FULL Thermobaricity
(a)
(b)
(c)
(d)
(e)
(f)
(g)
(h)
Depth (m)
0
500
1000
Latitude (°N)
−80
−60
−40
−20
0
20
40
60
10^{-5} m^{2}s^{-3}
6
3
0
−3
−6
3.0
1.5
0.0
−1.5
−3.0

Figure 11.

HIGH κ_n
HIGH - CTRL Temperature
HIGH - CTRL σ_2
LOW κ_n
LOW - CTRL Temperature
LOW - CTRL σ_2
MLT3D κ_n
MLT3D - CTRL Temperature
MLT3D - CTRL σ_2
FULL κ_n
FULL - CTRL Temperature
FULL - CTRL σ_2
(a)
(b)
(c)
(d)
(e)
(f)
(g)
(h)
(i)
(j)
(k)
(l)
Depth (m)
Latitude (°N)
m^2s^{-1}
°C
kgm^{-3}

Figure 12.

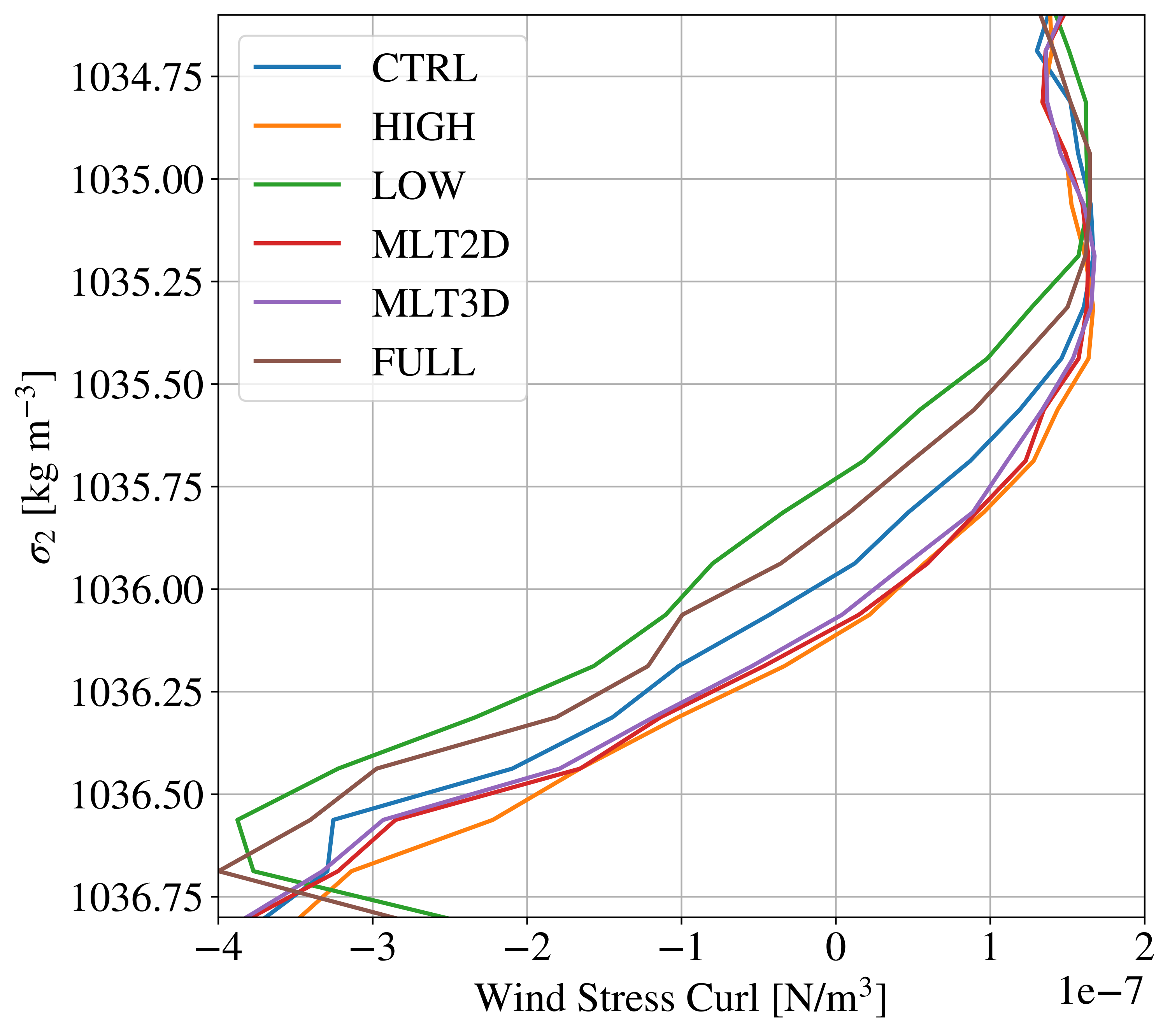
CTRL
HIGH
LOW
MLT2D
MLT3D
FULL
1034.75
1035.00
1035.25
1035.50
1035.75
1036.00
1036.25
1036.50
1036.75
σ_2 [kg m^{-3}]
−4
−3
−2
−1
0
1
2
1e−7
Wind Stress Curl [N/m^3]

Figure 13.

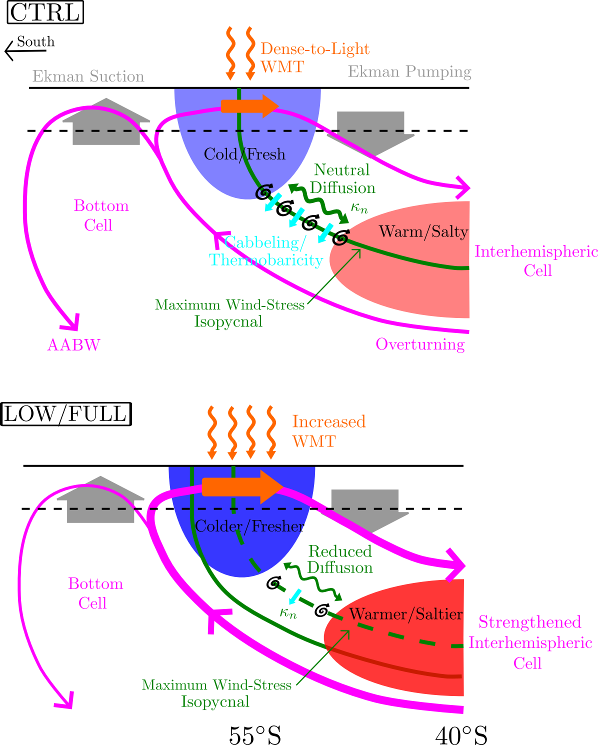
CTRL
South
Dense-to-Light
WMT
Ekman Suction
Ekman Pumping
Cold/Fresh
Neutral
Diffusion
κ_n
Bottom
Cell
Warm/Salty
Cabbeling/
Thermobaricity
Interhemispheric
Cell
Maximum Wind-Stress
Isopycnal
AABW
Overturning
LOW/FULL
Increased
WMT
Colder/Fresher
Reduced
Diffusion
Bottom
Cell
κ_n
Warmer/Saltier
Strengthened
Interhemispheric
Cell
Maximum Wind-Stress
Isopycnal
55°S
40°S

Figure 14.

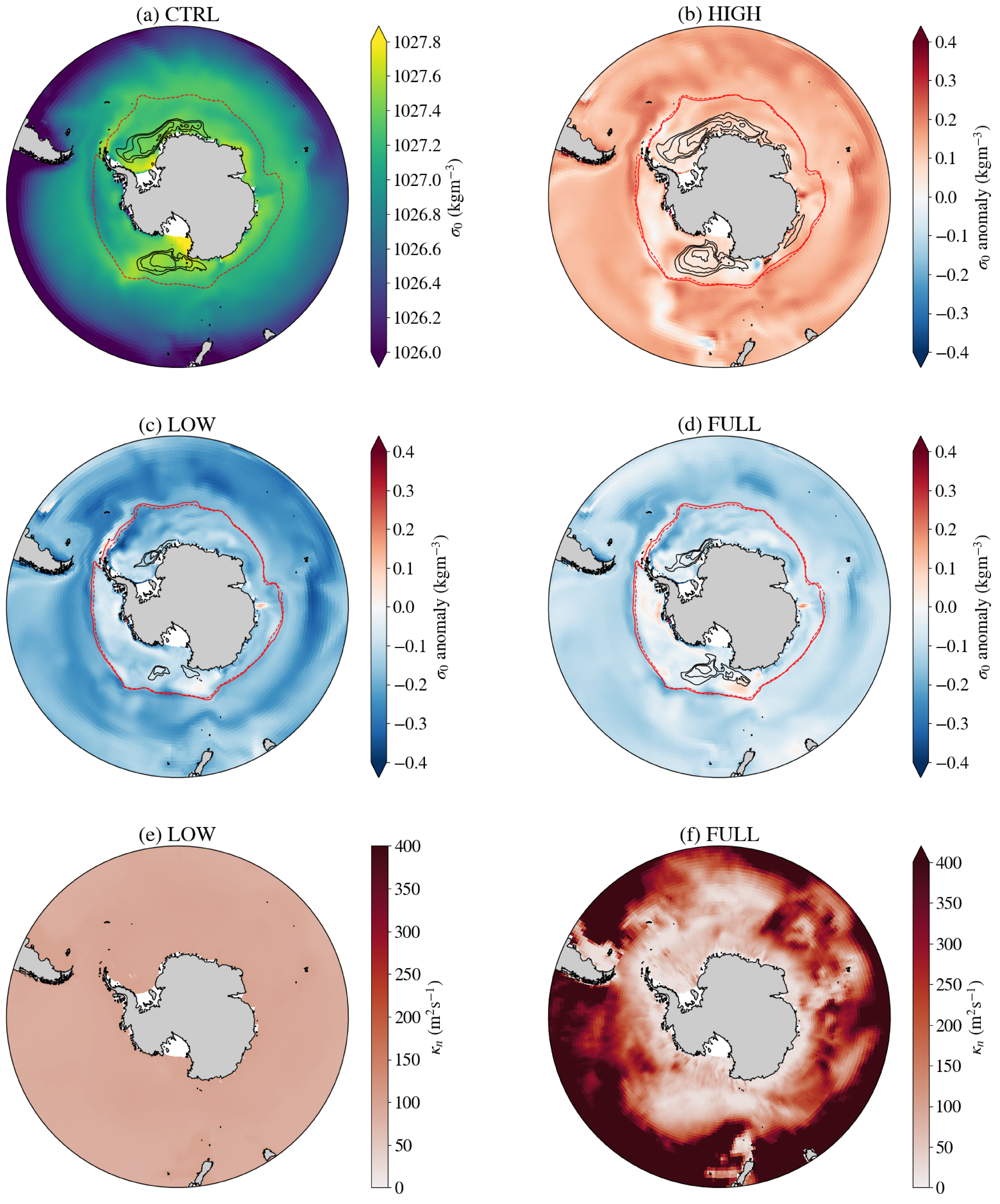

(a) CTRL
1027.8
1027.6
1027.4
1027.2
1027.0
1026.8
1026.6
1026.4
1026.2
1026.0
σ_0 (kgm^{-3})
(b) HIGH
0.4
0.3
0.2
0.1
0.0
−0.1
−0.2
−0.3
−0.4
σ_0 anomaly (kgm^{-3})
(c) LOW
σ_0 anomaly (kgm^{-3})
(d) FULL
σ_0 anomaly (kgm^{-3})
(e) LOW
400
350
300
250
200
150
100
50
0
κ_n (m^{2}s^{-1})
(f) FULL
κ_n (m^{2}s^{-1})